═══REVIEW COMMONS MANUSCRIPT═══

IMPORTANT:

- Manuscripts submitted to Review Commons are peer reviewed in a journal-agnostic way.
- Upon transfer of the peer reviewed preprint to a journal, the referee reports will be available in full to the handling editor.
- The identity of the referees will NOT be communicated to the authors unless the reviewers choose to sign their report.
- The identity of the referee will be confidentially disclosed to any affiliate journals to which the manuscript is transferred.

GUIDELINES:

- For reviewers: https://www.reviewcommons.org/reviewers
- For authors: https://www.reviewcommons.org/authors

CONTACT:

The Review Commons office can be contacted directly at: office@reviewcommons.org

AUTHORS: Isabela Aparecida Moretto[1*], Beatriz Rocha Ilidio Rodrigues[1*], Pedro Víctor-Carvalho[1], Maria das Graças de Souza Carvalho[1], Mariana Conceição da Silva[1], Fernando Valdivieso-Rivera[2], Giovanna Lopes de Araújo[3], Ana Paula Samogim[1], Lara Basseres Novais[1], Ingridi Rafaela de Brito[1], Guilherme Reis-de-Oliveira[3], Alan Gonçalves Amaral[1], Mariana Ozello Baratti[4], Fernanda Luisa Basei[5], Murilo Vieira Geraldo[6], Paulo Costa Carvalho[7], Marlon Dias Mariano Santos[8], Rosario Duran[8], Carlos Henrique Grossi Sponton[2], Jörg Kobarg[5], Fabio C. Gozzo[3], Hernandes F. de Carvalho[4], Andre Alexandre de Thomaz[4,9**], Aline Mara dos Santos[1,4**]

[1]Laboratory of Biological Physics and Cell Signaling, Institute of Biology, Department of Structural and Functional Biology, University of Campinas (UNICAMP), Campinas, Brazil.
[2]Research Center for Obesity and Comorbidities, University of Campinas (UNICAMP), Campinas, Brazil.
[3]Dalton Mass Spectrometry Laboratory, Institute of Chemistry, University of Campinas (UNICAMP), Campinas, São Paulo, Brazil.
[4]National Institute of Photonics Applied to Cellular Biology (INFABIC), University of Campinas (UNICAMP), Campinas, Brazil.
[5]Faculty of Pharmaceutical Sciences, University of Campinas (UNICAMP), Campinas, Brazil
[6]Laboratory of RNA Biology, Institute of Biology, University of Campinas (UNICAMP), Campinas, Brazil.
[7]Laboratory for Structural and Computational Proteomics, Carlos Chagas Institute, Fiocruz, Paraná, Brazil.
[8]Analytical Biochemistry and Proteomics Unit, Clemente Estable Institute of Biological Research, Institut Pasteur de Montevideo, Montevideo, Uruguay.
[9]Laboratory of Biological Physics and Cell Signaling, Quantum Electronics Department, Gleb Wataghin Physics Institute, University of Campinas, UNICAMP, Campinas, Brazil.

* These authors contributed equally to this work.

**Correspondence authors:

Aline Mara dos Santos
alinems@unicamp.br

Andre Alexandre de Thomaz
athomaz@unicamp.br

ARTICLE TITLE: Bclaf1 biomolecular condensates protect nuclear PTK2 from ubiquitin-proteasome system promoting cardiomyocyte survival during oxidative stress

SUMMARY

PTK2, a non-receptor tyrosine kinase, is essential for regulating pivotal cellular functions, including survival by reducing p53 levels and activating PI3K/AKT pathway. However, the mechanism underlying PTK2 stabilization during stress remained unclear. Here, we identified Bclaf1, a multifunctional protein known to stabilize partners, as a PTK2 interactor. Using advanced microscopy techniques, we identified nuclear Bclaf1 biomolecular condensates containing PTK2 in cardiomyocytes under oxidative stress. While PTK2 diffused through the nucleus was susceptible to ubiquitination, PTK2 sequestered in the Bclaf1 condensates was protected from the ubiquitin-proteasome system (UPS). The PTK2 ubiquitination site K926 was identified, and proteasome inhibition confirmed the UPS role in PTK2 homeostasis. Furthermore, the disruption of Bclaf1 biomolecular condensates culminates in PTK2 degradation, ultimately increasing p53 levels and activating apoptosis. Our findings support the role of Bclaf1 driving the formation of pro-survival nuclear condensates that sequester and stabilize PTK2, promoting cardiomyocyte survival during oxidative stress.

1. INTRODUCTION

Protein Tyrosine Kinase 2 (PTK2), also known as Focal Adhesion Kinase (FAK), is a multifunctional non-receptor tyrosine kinase involved in the regulation of primary cellular functions, including migration, mechanosensing, proliferation, and survival[1]. Under stress conditions, including mechanical and oxidative stress, PTK2 is rapidly activated through tyrosine 397 autophosphorylation[2,3,4]. Once phosphorylated, PTK2 recruits Src kinases to phosphorylate PTK2 on tyrosines 576 and 577 in the kinase activation loop, becoming fully activated[5,75,7]. Active PTK2 redistributes throughout the cytoplasm and nucleus to regulate several signaling pathways, such as PI3K-AKT-mTOR, MDM2-p53, and MEF2c-cJun, through its kinase activity or scaffolding function, promoting cell survival and hypertrophic growth of cardiomyocytes[2,8–12].

Several reports indicate nuclear PTK2 plays pivotal roles in the regulation of cell survival under stress[13–15]. Interestingly, cardiomyocyte PTK2-knockout mice showed increased susceptibility to apoptosis and cardiac dysfunction after doxorubicin (dox)-induced oxidative stress, while the myocyte-specific overexpression of PTK2 enhanced cell survival, providing

73 cardioprotection to dox treatment[13]. With oxidative stress generated by dox and the key role of
74 PTK2 to promote cardioprotection in mind, we reasoned that PTK2 must be protected and
75 stabilized in cardiomyocytes to promote survival during oxidative stress conditions. By an
76 unbiased immunoprecipitation coupled to mass spectrometry approach, we identified the Bcl-
77 2-associated transcription factor 1 (Bclaf1) as one of the most enriched interacting partners of
78 the FERM (four-point-one, ezrin, radixin, moesin)-PTK2 domain. Bclaf1 was previously
79 shown to function on the stabilization and proteostasis control of interacting-partners under
80 stress conditions[16,17]. However, the mechanism of protein stabilization by Bclaf1 remained
81 uncharacterized.

82 In this study, using a combination of biochemical and biophysical assays with super-resolution
83 microscopy, we identified nuclear Bclaf1 biomolecular condensates sequestering and
84 protecting PTK2 from the ubiquitin-proteasome system during doxorubicin-induced oxidative
85 stress, into submicron-scale membraneless organelles. Fluorescence Recovery After
86 Photobleaching (FRAP) revealed the ability of Bclaf1 to form biomolecular condensates via
87 liquid–liquid phase separation (LLPS). Knockdown of Bclaf1 resulted in increased PTK2
88 ubiquitination and degradation, and in cell death through activation of apoptosis pathways.
89 Moreover, a PTK2 lysine ubiquitination site was identified by mass spectrometry, while the
90 proteasome inhibition resulted in nuclear PTK2 accumulation and ubiquitination, confirming
91 the participation of the ubiquitin-proteasome system (UPS) on PTK2 homeostasis. Here, we
92 present a new PTK2 quality-control mechanism that operates during oxidative stress to
93 stabilize PTK2 and promote cell survival. Such mechanisms may promote cardioprotection
94 during stress conditions, including dox-induced cytotoxicity through oxidative stress.

95 **2. RESULTS**

96 **2.1 Bclaf1 is a novel nuclear binding partner of PTK2**

97 Protein-protein interactions regulate a wide range of cell functions during physiological or
98 pathological conditions, with its native structural conformation being essential to their proper
99 functionality[18,19]. To identify PTK2 stabilizing interacting partners, we conducted an
100 immunoprecipitation (IP) coupled to mass spectrometry. As a result, Bclaf1 was one of the
101 most enriched interacting partners of the FERM-PTK2 domain in HEK-293T cells (Fig. 1A;
102 Supplem. Fig. 1A). Interactome data bank analysis showed PTK2 and Bclaf1 linked to
103 overlapping pathways involved in cell signaling, however, this is the first time this interaction

104 was described (Fig. 1B; Supplem. Fig. 1B). Immunoprecipitation of PTK2 from lysates of
105 H9c2 cardiomyocytes confirmed the PTK2-Bclaf1 association in this cell type (Fig. 1C;
106 Supplem. Fig. 7A). When Bclaf1 was immunoprecipitated, PTK2 also was found to co-
107 precipitate (Fig 1D; Supplem. Fig. 7A). This validates the PTK2-Bclaf1 interaction in H9c2
108 cardiomyocytes.

109 Next, to explore the subcellular distribution of PTK2 and Bclaf1 in cardiomyocytes, super-
110 resolution images were acquired by Structured Illumination Microscopy (SR-SIM). Figure 1E
111 shows PTK2 distributed throughout the cytoplasm and nucleus and Bclaf1 mostly localized at
112 the nucleus. On the right panel, overlapped channels show colocalization areas of PTK2 and
113 Bclaf1. Two regions were highlighted, and Z-stack analysis showed evidence of PTK2-Bclaf1
114 interactions in the nuclear compartment of H9c2 cardiomyocytes (Fig. 1F-G). It was noticed
115 that PTK2 and Bclaf1 displayed a diffuse distribution in the nucleus and colocalized in multiple
116 points through the examined stacks. Proximity Ligation Assay (PLA) confirmed the PTK2-
117 Bclaf1 direct interaction (Fig. 1H) establishing Bclaf1 as a new PTK2 interactor.

A

Entrez Gene Name	Sequence	XCorr	*m/z* (Da)	Charge
Protein tyrosine kinase 2	SEEVHWLHVDMGVSSVR	4.68	983.97156	2
	YELAHPPEEWKYELR	4.09	980.48560	2
	QFANLNREESILK	3.78	781.41711	2
	FFEILSPVYR	3.22	635.84259	2
	SNYEVLEK	2.90	491.24432	2
	KGMLQLK	2.67	409.24841	2
	KLIQQTFR	2.61	517.30762	2
	IVDSHKVK	2.53	463.27249	2
	LGcLEIR	2.05	860.46063	1
	SYWEMR	1.96	871.37262	1
BCL-associated transcription factor 1	MAPVPLDDSNRPASLTK	4.29	906.46552	2
	SSATSGDIWPGLSAYDNSPR	4.16	1040.9810	2
	SQEEPKDTFEHDPSESIDEFNK	3.94	870.04382	3
	GTFHDDRDDGVDYWAK	3.25	948.90594	2
	LKDLFDYSPPLHK	2.86	524.94977	3
	SSFYPDGGDQETAK	2.85	751.32166	2
	LLASTLVHSVK	2.80	584.35480	2
	KSVLADQGK	2.66	945.52942	1

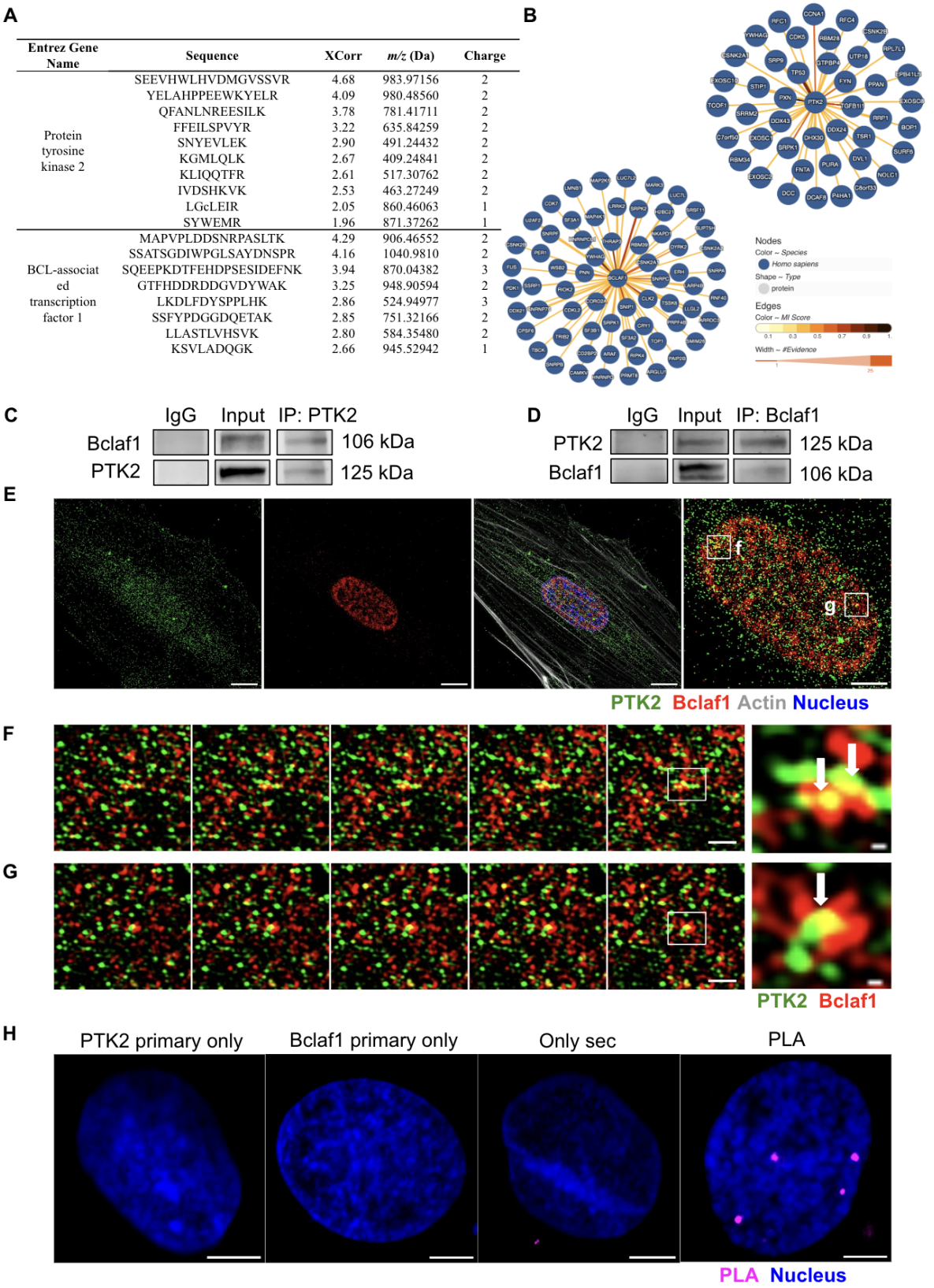

Figure 1. Bclaf1 is a binding partner of PTK2. A. Data from mass spectrometry of HEK-293T cells demonstrating Bclaf1 on Flag-FERM-PTK2 immunoprecipitate. **B.** Interaction networks of PTK2 and Bclaf1 on HEK293T obtained from IntAct (https://www.ebi.ac.uk/intact/home), including association and physical association. **C-D.** Bclaf1 immunoblots of PTK2 immunoprecipitated from control H9c2 extracts confirming the

PTK2-Bclaf1 interaction, and vice versa. PTK2 (C) and Bclaf1 (D) served as loading control. **E.** Super-resolution images of H9c2 cells on basal conditions, stained for PTK2, Bclaf1, actin, and nucleus. Scale bar = 10 µm. Nucleus zoomed image scale bar = 5 µm. **F-G.** Z-stack slices of nuclear planes showing the association of PTK2 with Bclaf1 (arrows). Scale bar = 1 µm. Zoomed images scale bar = 0.1µm. **H.** Proximity Ligation Assay (PLA) demonstrating the interaction between PTK2 and Bclaf1 in untreated cells. Scale bar: 5 µm. Green: PTK2; Red: Bclaf1; Blue: nucleus; Grey: actin; magenta: PLA.

2.2 PTK2 and Bclaf1 are responsive to oxidative stress generated by doxorubicin, forming nuclear condensates

To investigate whether PTK2 and Bclaf1 are sensitive to oxidative stress (OS) generated by doxorubicin (dox), H9c2 cells were treated with this compound (12h; 1 µM) and analyzed by SR-SIM and western blotting. Dox treatment induced PTK2 nuclear accumulation and a rearrangement of Bclaf1 and PTK2 into prominent nuclear biomolecular condensates (Fig. 2A-B), which are non-membrane-bound biological structures with a physically defined boundary generated by surface tension[20]. Furthermore, we observed that dox treatment induces PTK2 autophosphorylation at tyrosine 397 residue, an essential event for its switch to an open and active conformation, culminating in PTK2 activation in the cell nuclei (Fig. 2C-D). Further analysis of cytosolic and nuclear extracts confirmed the subcellular distribution of PTK2 and its activation in the nuclear compartment (Fig. 2E-F; Supplem. Fig. 7B-C). The autophosphorylation of tyrosine 397 induces PTK2 conformational changes which culminates in the exposition of protein-protein interactions sites and in the kinase domain activation[21]. These data indicate that PTK2 and Bclaf1 are sensitive to dox treatment and may regulate nuclear events to modulate cell behavior and fate during OS stimuli.

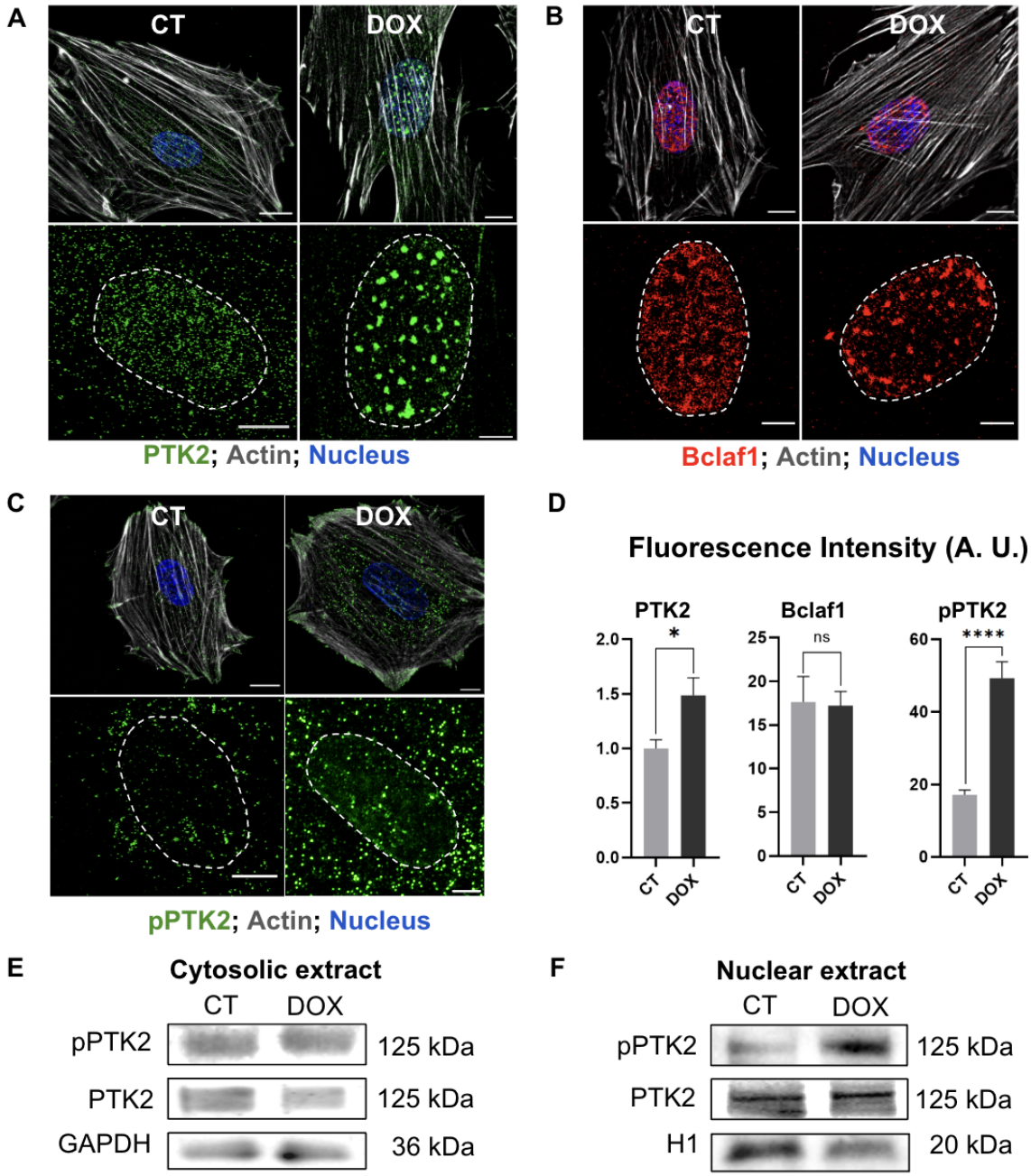

Figure 2. PTK2 and Bclaf1 are responsive to oxidative stress. **A-B.** Immunofluorescence images of H9c2 cardiomyocytes showing PTK2 and Bclaf1 reorganization in dot-like structures after dox treatment, respectively. **C.** Immunofluorescence images of pY397-PTK2 (pPTK2) showing nuclear PTK2 activation after dox treatment. **D.** Bar graphs show the nuclear fluorescence intensity of PTK2, Bclaf1, and pPTK2 on basal conditions and after dox treatment. Asterisks means statistical significance, while ns means $P > 0.05$; * means $P \leq 0.05$; ** means $P \leq 0.01$; *** means $P \leq 0.001$ and **** means $P \leq 0.0001$. **E-F.** pY397-PTK2, PTK2, GAPDH, and Histone H1 (H1) specific immunoblots of cytoplasmic and nuclear extract of H9c2 control or treated with dox. Dox treatment: 1 µM; 12h. Green: PTK2 and pPTK2; Grey: Actin; Red: Bclaf1; Blue: nucleus. Scale bar = 5 µm. Scale bar of zoomed images = 3 µm.

159

160 We next examined whether the PTK2-Bclaf1 interaction persists during dox-induced stress.
161 Co-IP assays revealed an association of Bclaf1 to the PTK2 immunoprecipitate, and vice versa
162 (Fig. 3A-B; Supplem. Fig. 7A), confirming the PTK2-Bclaf1 interaction in H9c2
163 cardiomyocytes under dox-induced OS. Super-resolution images showed a high colocalization
164 pattern of PTK2 and Bclaf1 nuclear condensates (Fig. 3C-D), indicating a very strong
165 interaction. Even in non-dot-like regions PTK2 and Bclaf1 co-localize with a diffuse pattern.
166 Furthermore, because our image resolution is ~80-100 nm, it was possible to resolve the
167 internal structure of these condensates (Fig. 3C-E), which areas ranged from 200 to 700 nm^2.
168 For instance, in Figure 3D, the PTK2 condensate presents 3 bright peaks (arrowhead), which
169 represent different internal concentration regions. On the other hand, the Bclaf1 condensates
170 present a cavity containing PTK2. The cavity in the Bclaf1 condensates was occupied by the
171 bright peaks of PTK2, which points to an isolation of PTK2 inside the Bclaf1 condensates. The
172 PTK2-Bclaf1 condensate spatial disposition was confirmed by 3D images and fluorescence
173 line profile plot (Fig. 3E-F). PLA experiments demonstrated a direct interaction of PTK2 and
174 Bclaf1 in cells under dox-induced stress (Fig. 3G). Moreover, differentiated cardiomyocytes
175 were able to form Bclaf1 condensates containing PTK2 when treated with dox (Supplem. Fig.
176 2A-C). The PTK2-Bclaf1 biomolecular condensates exhibited different sizes and
177 morphologies, from simple spherical shapes to complex structures with non-spherical
178 topologies, which may reflect the presence of multiphase structures or different stages in their
179 maturation[20,22,23]. Our results demonstrated the assembly of PTK2-Bclaf1 nuclear condensates
180 is an overall response to OS on both precursor and differentiated cardiomyocytes.

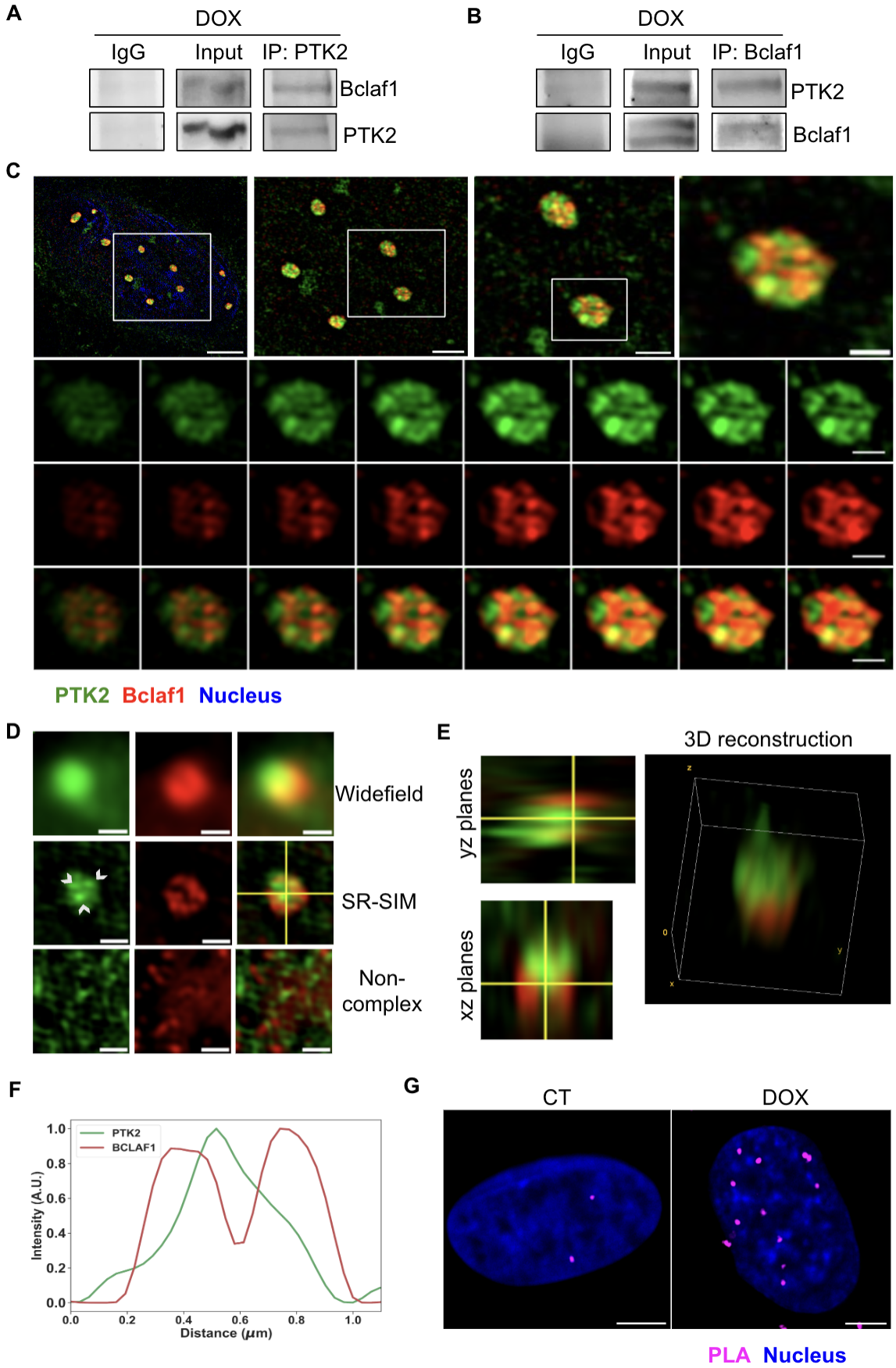

181

182 **Figure 3. Oxidative stress induces PTK2 and Bclaf1 association into nuclear biomolecular**

183 **condensates. A-B.** Bclaf1 immunoblots of PTK2 immunoprecipitate from dox-treated H9c2
184 cardiomyocytes extracts, and vice versa. PTK2 (A) and Bclaf1 (B) served as input loading
185 control. **C.** Immunofluorescence images of dox-treated cardiomyocytes showing the
186 rearrangement of Bclaf1 into nuclear condensates containing PTK2. Below, Z-stack from
187 nuclear planes, demonstrating the association of PTK2 and Bclaf1 in different planes. Scale
188 bar of upper panels = 5 µm, 1 µm, 2 µm, and 0.5 µm, respectively. Scale bar of Z-stack images
189 = 0.5 µm. **D.** PTK2-Bclaf1 condensate image showing strong colocalization in contrast with a
190 no-complex region. Arrowhead shows the 3 PTK2 bright peaks. Scale bar = 0.5 µm. **E.**
191 Orthogonal Z projection showing yz planes, xz planes and 3D reconstruction of the Bclaf1
192 biomolecular condensate containing PTK2 shown in "d". **F.** Fluorescence line profile plot of
193 the yellow horizontal line in (E) showing PTK2 inside the Bclaf1 condensate. Green: PTK2;
194 Red: Bclaf1; Blue: nucleus. Dox treatment: 1 µM; 12h. **G.** Proximity Ligation Assay showing
195 increased interaction between PTK2 and Bclaf1 after dox treatment. Scale bar = 5 µm.

196 **2.3 PTK2 interacts with Bclaf1 via liquid-liquid phase transition**

197 To better characterize the PTK2-Bclaf1 interaction, structural predictions and *in vivo*
198 experiments were employed. AlphaFold 3[24,25]analyses revealed Bclaf1 as an intrinsically
199 disordered protein (IDP) presenting an inner core of 4 alpha helices with flexible long loops
200 surrounding it (Fig. 4A). The Predict Alignment Error (PAE) reflects this spatial conformation
201 by having low value errors only on its diagonal in the PAE matrix. The unfolded pattern
202 predicted for Bclaf1 indicates its ability to easily accommodate the docking of partner proteins,
203 which corroborate its stabilization function described previously for HIF1-α and PD-L1[16,17,26].
204 Otherwise, PTK2 presents a much more stable predicted structure (Fig. 4B). The three main
205 domains, which had their individual structure characterized, present low PAE scores meaning
206 their positions are very accurate. There is an intrinsically disordered region (IDR) in the N-
207 terminal portion of the FERM domain and a longer IDR linking Kinase and FAT domains,
208 compressed by Q686 to S934 residues, containing one alpha-helix (Q805-S832) positioned in
209 the interface between the kinase and FAT domains. Pursuing Bclaf1 and PTK2 models, we
210 next used the docking tool of AlphaFold3 to predict the PTK2-Bclaf interacting-models (Fig.
211 4C; Supplem. Fig. 3). From this prediction we could see an intimate association between Bclaf1
212 and PTK2, where Bclaf1 flexible loops can involve the entire structure of PTK2. The molecular
213 mechanisms by which Bclaf1 interacts and stabilizes protein partners is unknown[16,27], however,
214 the results obtained from AlphaFold3 combined with its ability to form nuclear punctate
215 structures raised the hypothesis that Bclaf1 forms biomolecular condensates via liquid-liquid
216 phase separation (LLPS), which increase the mobility of client proteins. During LLPS,
217 biomolecules condense from the surrounding cellular environment into distinct membraneless
218 compartments. This process concentrates proteins within the condensates, effectively
219 increasing their binding affinity and minimizing competition with other interactors[28,29].

220 To investigate the propension of Bclaf1 and PTK2 to interact via LLPS, we calculated the
221 scores for liquid-liquid phase separation of Bclaf1, PTK2 and PTK2-Bclaf1 complex using two
222 different methods, FuzDrop[27–29] and PSPRedictor[30] (Fig. 4D). As expected, the Bclaf1 scores
223 were close to 1 (FuzDrop = 0.9995, PSPredictor = 0.9968) meaning it is prone to undergo
224 LLPS. PTK2 presented lower scores (FuzDrop = 0.5332, PSPRedictor = 0.1543), indicating a
225 low propensity for self-driven phase separation. Nevertheless, the intrinsically disordered N-
226 terminal region and the linking between the Kinase and FAT domain has a high predicted
227 propensity for phase separation according to the FuzDrop score ~ 0.99, suggesting these
228 regions might contribute to PTK2 LLPS when induced by an interacting partner. Finally, the
229 scores for PTK2-Bclaf1 complex (PSPRedictor, FuzDrop) indicated a high probability to
230 condensate via LLPS. The number of residues with a high probability (Predicted Drip
231 Propensity > 0.5) of promoting liquid-liquid phase separation align with the data above. Both
232 PTK2 and Bclaf1 have residues with high LLPS probabilities, however, Bclaf1 clearly has a
233 greater number of residues with higher droplet formation probabilities (Fig. 4E).

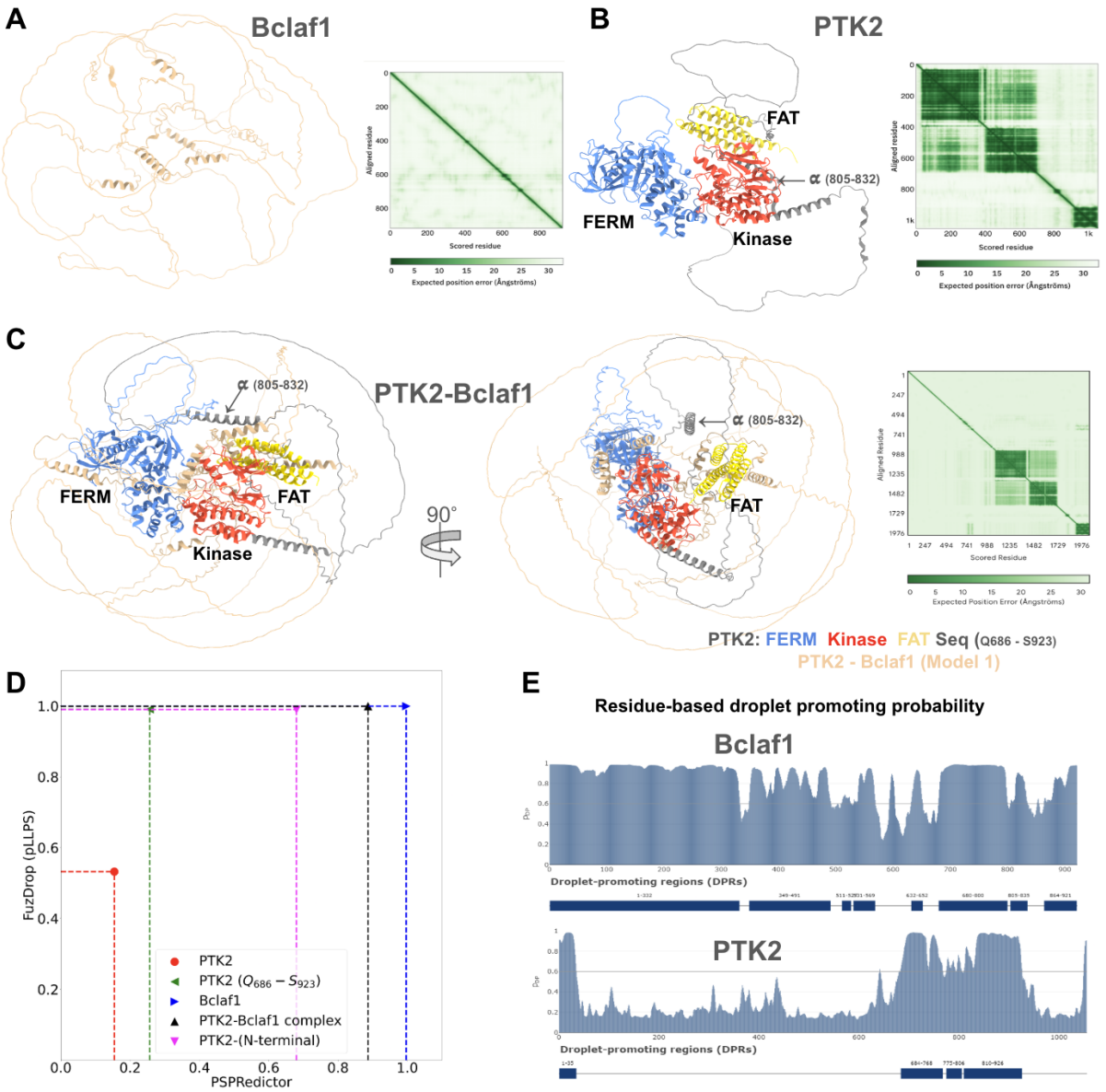

Figure 4. Computational predictions of PTK2-Bclaf1 interaction. A. The structure of Bclaf1, an intrinsically disordered protein (IDP), with an inner core of 4 alpha helices and flexible long loops was obtained using AlphaFold3. PAE matrix indicates low error values only on the diagonal, reflecting the Bclaf1 unfolding nature. **B.** PTK2 structure, with three main domains and a long intrinsically disordered region (IDR) linking the Kinase and FAT domains obtained by AlphaFold3 platform is shown. PAE matrix shows the predicted error in Angstroms. **C.** Predicted PTK2-Bclaf1 modeled using AlphaFold3 docking tool and PAE matrix, indicating low error values for the PTK2 domains and a higher error value for the IDR. Interfaces of PTK2-Bclaf1 interaction with intermediate error values are shown. **D.** LLPS propensity scores for Bclaf1, PTK2, IDR PTK2-N-terminal, Q686 - S923 IDR PTK2 sequence, and the PTK2-Bclaf1 complex obtained using FuzDrop and PSPredictor. **E.** Residue-based droplet promoting probability of PTK2 and Bclaf1 obtained by FuzDrop.

To validate the LLPS prediction data we performed Fluorescence Recovery after Photobleaching (FRAP). When a protein is transitioned to LLPS its diffusion coefficient

249 increases, reflecting a higher mobility in this phase[31,32]. In Figure 5A we plotted the fitted
250 FRAP curves showing an increased diffusion of EGFP-Bclaf1 and EGFP-PTK2 in the
251 condensate in contrast with the low mobility of these proteins outside the condensates,
252 confirming that PTK2-Bclaf1 complex condensate via LLPS (Fig. 5B). We also performed
253 Fluorescence-Lifetime imaging microscopy (FLIM)[33]. Due to the presence of two different
254 phases of the same protein, the fluorescence lifetime changes reflecting this aspect. Bclaf1
255 showed an increased lifetime on condensate (1.095 ± 0.022 ns) relative to nucleus regions
256 (0.935 ± 0.062 ns) and PTK2 also presented an increased lifetime fluorescence (1.028 ± 0.026
257 ns) compared to non-condensate molecules (0.854 ± 0.020 ns) (Fig. 5C-D). This data showed
258 that Bclaf1 and PTK2 present higher mobility inside the biomolecular condensates and a
259 different fluorescence lifetime as well, indicating a different phase for these proteins inside the
260 condensates.

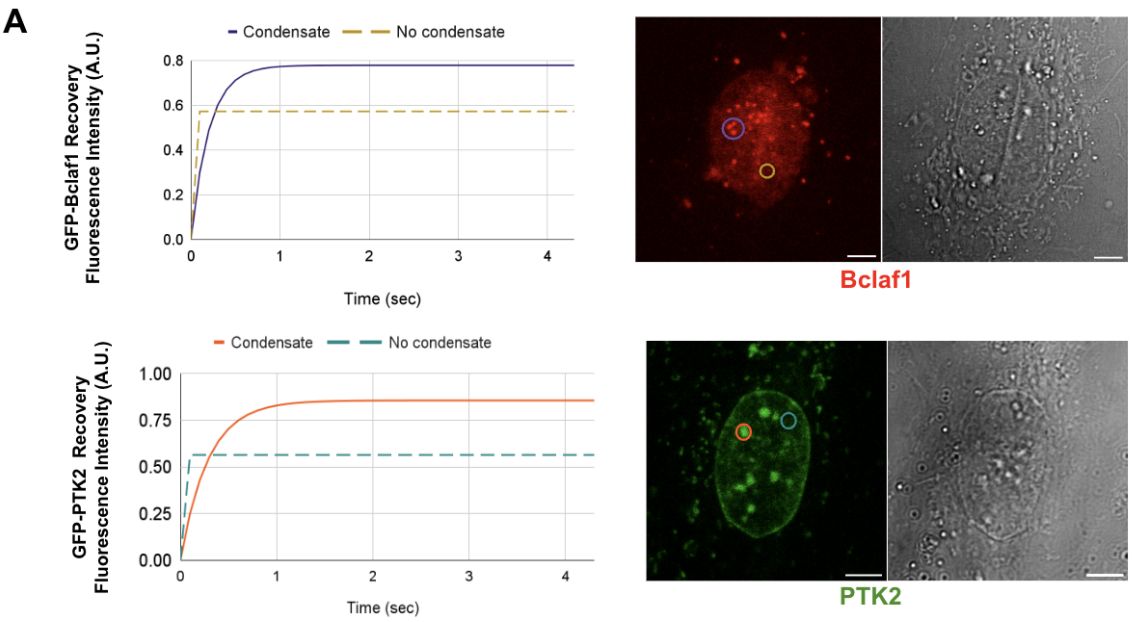

B

Protein	Treatment	Mobile Fraction, μ	b	*n*
Bclaf1	Condensate	0.78 ± 0.019	4.92 ± 0.52	15
	No Condensate	No recovery	No recovery	-
PTK2	Condensate	0.86 ± 0.04	3.46 ± 0.82	10
	No Condensate	No recovery	No recovery	-

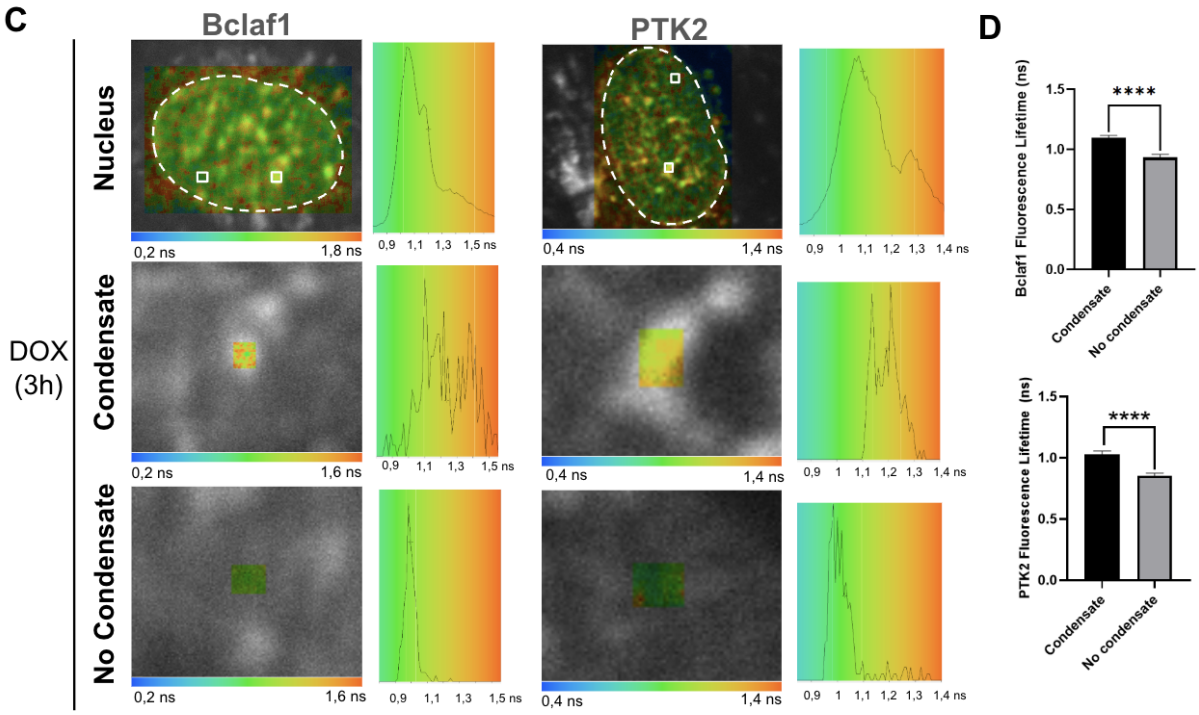

Figure 5. Bclaf1 and PTK2 undergo liquid-liquid phase separation to form submicron membraneless organelles. A. FRAP fitted graphs of condensate and out of condensate nuclear regions of H9c2 cells transfected with EGFP-Bclaf1 and EGFP-PTK2, in individual

experiments. Bclaf1 and PTK2 present higher diffusion on condensate regions in relation to non-condensate areas. Images show the fluorescence and differential interference contrast (DIC) images of EGFP-Bclaf1 and EGFP-PTK2 expressing cells. Scale bar = 5 μm. **B.** Mobile fraction and constant of the fluorescence recovery rate for Bclaf1 and PTK2. **C.** Lifetime images of H9c2 cells expressing GFP-Bclaf1 or GFP-PTK2 fluorescent proteins. **D.** Bar graph of EGFP-Bclaf1 and EGFP-PTK2 fluorescence lifetime in condensates and no condensate areas. Asterisks means statistical significance, while ns means $P > 0.05$; * means $P \leq 0.05$; ** means $P \leq 0.01$; *** means $P \leq 0.001$ and **** means $P \leq 0.0001$.

2.4 Hsp70 activity and oxidative stress levels modulate the LLPS-mediated formation of PTK2-Bclaf1 condensates

Despite the acknowledgment on LLPS physical properties, the molecular chaperone role on the phase transition remains unclear. To verify whether Hsp70 activity modulates the dynamics of the PTK2-Bclaf1 biomolecular condensates, we performed SR-SIM and FRAP combined with chemical inhibition of Hsp70 (VER-155008; 50 μM). Firstly, the cells were incubated with dox for 1, 3, 6, and 12 h (1 μM) and analyzed by triple-labeling SR-SIM. As depicted on Figure 6A the clusterization of Hsp70 with PTK2 starts as early as 1 h of dox treatment. After 3 h, the PTK2-Bclaf1 condensates were clearly visualized, along with the presence of Hsp70, which was found to be associated with the condensates over all the subsequent times, indicating an active participation of Hsp70 on their dynamic. Secondly, to confirm the Hsp70 contribution to this process, cells were examined by FRAP after being transfected with EGFP-Bclaf1 or with EGFP-PTK2 and co-treated with dox (3 h) and VER-155008 (1 h). Hsp70 inhibition reduced the diffusion of Bclaf1 to the early formed condensate area, as indicated by the reduction of the *b* coefficient. Conversely, the diffusion of PTK2 was not affected by the inhibition of Hsp70 (Fig. 6B), indicating the dynamic of PTK2 can be modulated by other disaggregase, such as AAA+ATPases. Further studies could confirm this hypothesis. Together, our data confirmed the role of Hsp70 in regulating the mobility of Bclaf1 within the biomolecular condensate, providing a deeper understanding of the dynamic behavior of these nuclear membraneless organelles during OS.

Next, we sought to analyze the relationship of PTK2-Bclaf1 liquid-liquid phase separation with the excess of reactive oxygen species (ROS) generated by dox. CellROX assays were performed on control and dox-treated cardiomyocytes. The cells were incubated for 1, 3, 6, and 12 h with dox and examined by fluorescence microscopy after the incubation with CellROX reagent. Image analysis showed a correlation of OS levels and the biomolecular condensate formation. The level of ROS increased between 3 and 6 h of dox treatment, and started to

299 reduce at 12 h. Interestingly, the PTK2-Bclaf1 condensates appear after 3 h of treatment, such
300 as the OS, with a peak on the number of condensates at 6 h and a decrease at 12 h of dox
301 treatment (Fig. 6E). MTT assays demonstrated a preservation of cell viability until 6h of dox
302 treatment, which was reduced after 12 h by ~ 20 % in relation to control cells (Fig. 6F),
303 indicating LLPS is induced by OS and functions to enhance cell survival during stress
304 conditions. To analyze whether apoptosis pathways were activated during this event, we
305 performed western blot assays to p53, phospho-p53 and cleaved caspase-3, which were not
306 altered on adhered cardiomyocytes, only a tendency for a p53 increase was observed after 12
307 h of dox treatment (Fig. 6G; Supplem. Fig. 4B; Supplem. Fig. 7D). Taken together, this data
308 confirmed that Bclaf1 and PTK2 undergoing LLPS is a response to the oxidative stress induced
309 by dox as a mechanism to enhance cell survival.

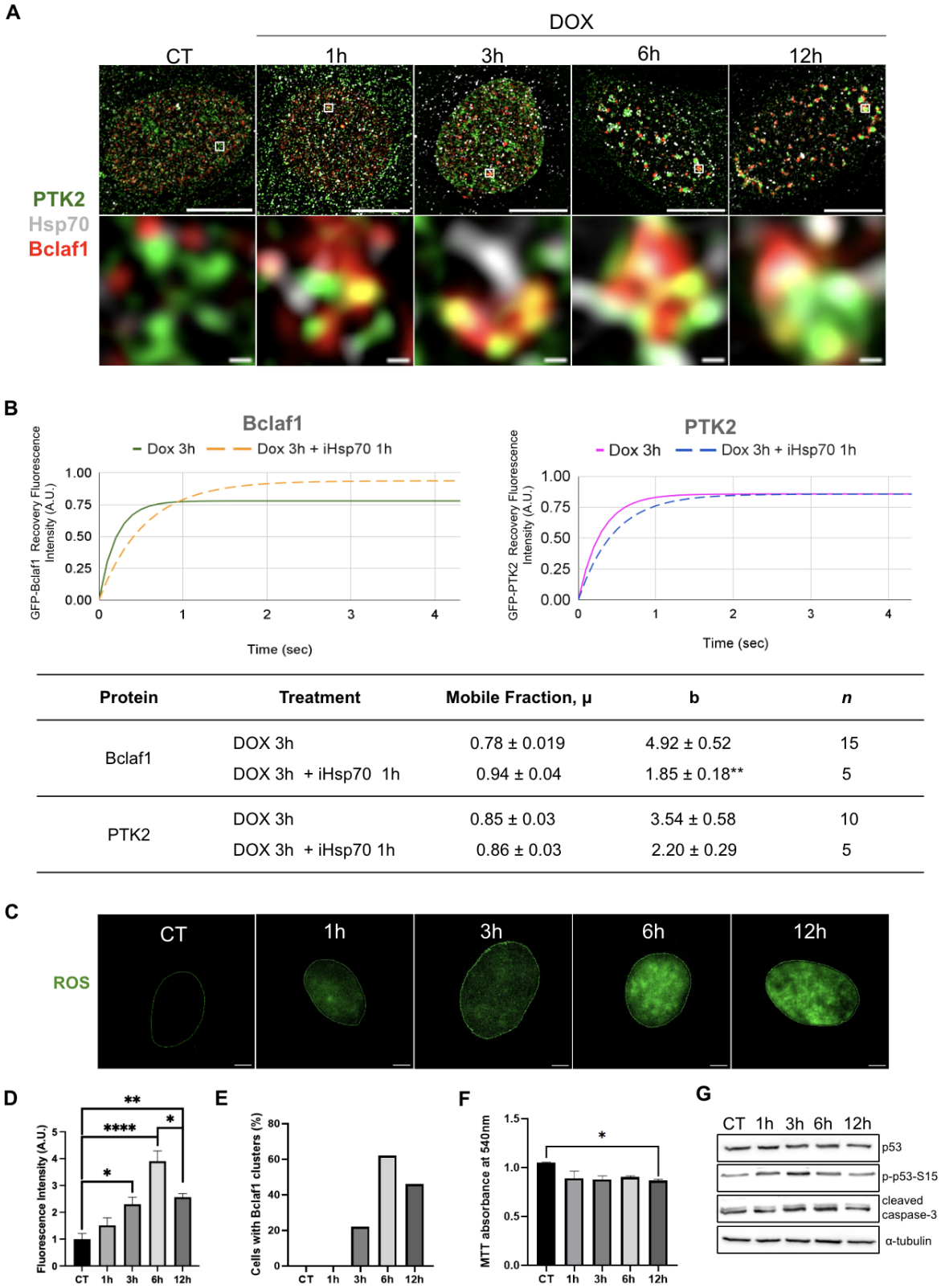

Protein	Treatment	Mobile Fraction, μ	b	*n*
Bclaf1	DOX 3h	0.78 ± 0.019	4.92 ± 0.52	15
	DOX 3h + iHsp70 1h	0.94 ± 0.04	1.85 ± 0.18**	5
PTK2	DOX 3h	0.85 ± 0.03	3.54 ± 0.58	10
	DOX 3h + iHsp70 1h	0.86 ± 0.03	2.20 ± 0.29	5

Figure 6. Hsp70 and oxidative stress modulates the condensate formation. A. Super-resolution images of H9c2 cardiomyocytes showing the colocalization of Hsp70 (gray) with PTK2 (green) and Bclaf1 (red) on the condensate region. Scale bar = 10 μm. Scale bar of zoomed images = 0.5 μm. **B.** FRAP graph showing the fluorescence recovery after photobleaching of EGFP-Bclaf1 and EGFP-PTK2 after Hsp70 inhibition (iHsp70). Asterisks

demonstrates statistical significance, while ns means P > 0.05; * means P ≤ 0.05; ** means P ≤ 0.01; *** means P ≤ 0.001 and **** means P ≤ 0.0001. **C.** Time-course experiments using CellROX show an increasing oxidative stress during dox treatment. Scale bar = 5 µm. **D.** Bar Graph shows the percentage of cells with Bclaf1 clusters from control (CT) to 12h of dox treatment, as indicated (n=80 for CT, n=59 for 1h, n=94 for 3h, n=76 for 6h, and n=91 for 12h). **E.** Bar graph shows the MTT absorbance at 540 nm. **F.** Western Blot images of p53, p53 phosphorylated at Ser 15 (p-p53-S15), and cleavage caspase-3. α-Tubulin served as loading control. Bar Graphs are shown in Supplementary Figure 4.

2.5 Bclaf1 biomolecular condensates protects PTK2 from the ubiquitin-proteasome system during dox-induced oxidative stress

Oxidative stress occurs when there is an imbalance between the production of reactive oxygen species and the intracellular antioxidant defenses, which can lead to potential damage, destabilizing proteins and other cell components[34,35]. As biomolecular condensates function in stress conditions by sequestering and stabilizing proteins[28,36,37], we reasoned that Bclaf1 condensates were likely to be molecularly relevant to stabilize and protect PTK2 from aggregation and ubiquitination in the context of OS. To explore this hypothesis, we examined whether PTK2 localized into the Bclaf1 biomolecular condensate is less susceptible to ubiquitination in relation to that diffusely dispersed in the nucleus. Triple-staining SR-SIM and image analysis showed that PTK2 diffusely disposed throughout the nucleus colocalizes with ubiquitin dot-staining, indicating the action of the ubiquitin-proteasome system (UPS) in sorting and degradation of PTK2 during dox-induced OS (Fig. 7A; panel 1). However, PTK2 localized within the Bclaf1 condensates showed very low ubiquitination (Fig. 7A; panel 2), indicating a role of Bclaf1 to protect PTK2 from the UPS during OS. Next, we calculated the correlation of the integrated fluorescence of each channel. After automatic delimitation and identification of the Bclaf1 condensates area on Fiji software, a Python code calculated the Pearson correlation coefficient for the integrated fluorescence between PTK2, Bclaf1, and Ubiquitin channels. Higher values of this coefficient indicate the presence of both proteins at a given region, while negative values indicate they are anticorrelated and zero indicates no correlation. Figure 7B shows that PTK2 and Bclaf1 have a higher correlation coefficient (0.89 ± 0.02; AVG ± SEM) than PTK2 and Ubiquitin (0.68 ± 0.05). This shows that if PTK2 is sequestered at the biomolecular condensate it is less prone to be ubiquitinated.

As diffuse PTK2 presents a higher chance of being ubiquitinated, we used western blotting and RT-qPCR assays to investigate whether PTK2 levels were reduced after dox-induced OS. Accordingly, our data confirmed a reduction in PTK2 protein levels in dox-treated cells (Fig.

350 7C; Supplem. Fig. 7E), while RT-qPCR analysis revealed no significant change in PTK2
351 mRNA levels (Fig. 7D), pointing to an increase in PTK2 degradation. To analyze PTK2 quality
352 control during dox-induced OS, soluble (S) and insoluble (P) extracts were prepared. Western
353 blot analysis of control S and P samples demonstrated the presence of the 125 kDa band,
354 corresponding to PTK2 Full Length (PTK2-FL) and the characteristic proteolytic fragments
355 derived from calpain or caspase 3 cleavage[4,36] (Fig. 7E). After dox treatment, the abundance of
356 PTK2-FL in the soluble fraction decreased, while the proportion of the 50 kDa fragment
357 increased, suggesting increased fragmentation of PTK2 during dox exposure. Interestingly,
358 reduced levels of PTK2-FL and its fragments were observed in the insoluble fraction,
359 suggesting that they are primarily soluble and readily accessible for ubiquitination and
360 degradation by the UPS. Corroborating this hypothesis, we observed ubiquitination over PTK2
361 corresponding bands, mainly in the soluble fraction of cells treated with dox (Fig. 7E),
362 confirming that the decreased levels of PTK2 during dox treatment are related to its
363 ubiquitination and proteolytic degradation. Together, these data suggest that PTK2 is
364 ubiquitinated and degraded during dox-induced OS, while Bclaf1 condensates counterbalances
365 this process protecting nuclear PTK2 from the UPS.

366 To get more information about PTK2 stability and ubiquitination after dox treatment, H9c2
367 cells were treated with dox for 12h and recovered for 36h in a dox-free medium. SR-SIM
368 analysis showed the presence of PTK2-Bclaf1 condensates and also the accumulation of
369 ubiquitinated-PTK2 aggregates in the nuclear compartment after an extended exposition to OS,
370 confirming an ongoing effect of the oxidative damage and PTK2 destabilization and
371 ubiquitination (Fig. 7F; Supplem. Fig. 5). Taken together, our results suggest a dynamic
372 mobility of PTK2 to the Bclaf1 biomolecular condensates, where this kinase is protected from
373 the UPS action. However, PTK2 diffusing through the nucleus can be destabilized by OS
374 resulting in its ubiquitination and degradation or accumulation in amorphous nuclear
375 aggregates (Fig. 7G). Next, to gather more information on the control of PTK2 proteostasis,
376 H9c2 cardiomyocytes were treated with the proteasome inhibitor MG132 to induce a disruption
377 of UPS-dependent proteostasis during dox-induced OS. Western blot analysis shows an
378 increase in the overall ubiquitination after MG132 treatment (Fig. 7H). As expected, our super-
379 resolution images showed an extensive accumulation of ubiquitinated PTK2 in the nuclei (Fig.
380 7I). Additionally, Bclaf1-biomolecular condensates were abundant after the inhibition of the
381 proteasome, indicating Bclaf1 LLPS increased after the co-treatment with dox and MG132.
382 However, the physical characteristics of these condensates were not assessed. In Figure 7I, a

383 zoomed nuclear region is shown on orthogonal view, demonstrating the ubiquitin presence in
384 PTK2 aggregates and the absence of the Bclaf1 biomolecular condensates (panel 1), confirming
385 the participation of proteasome degradation on PTK2 quality control. Furthermore, a prominent
386 cell death was observed for cardiomyocytes co-treated with dox and MG132 (Fig. 7J),
387 reflecting the severe effect of impaired proteostasis combined with oxidative damage.

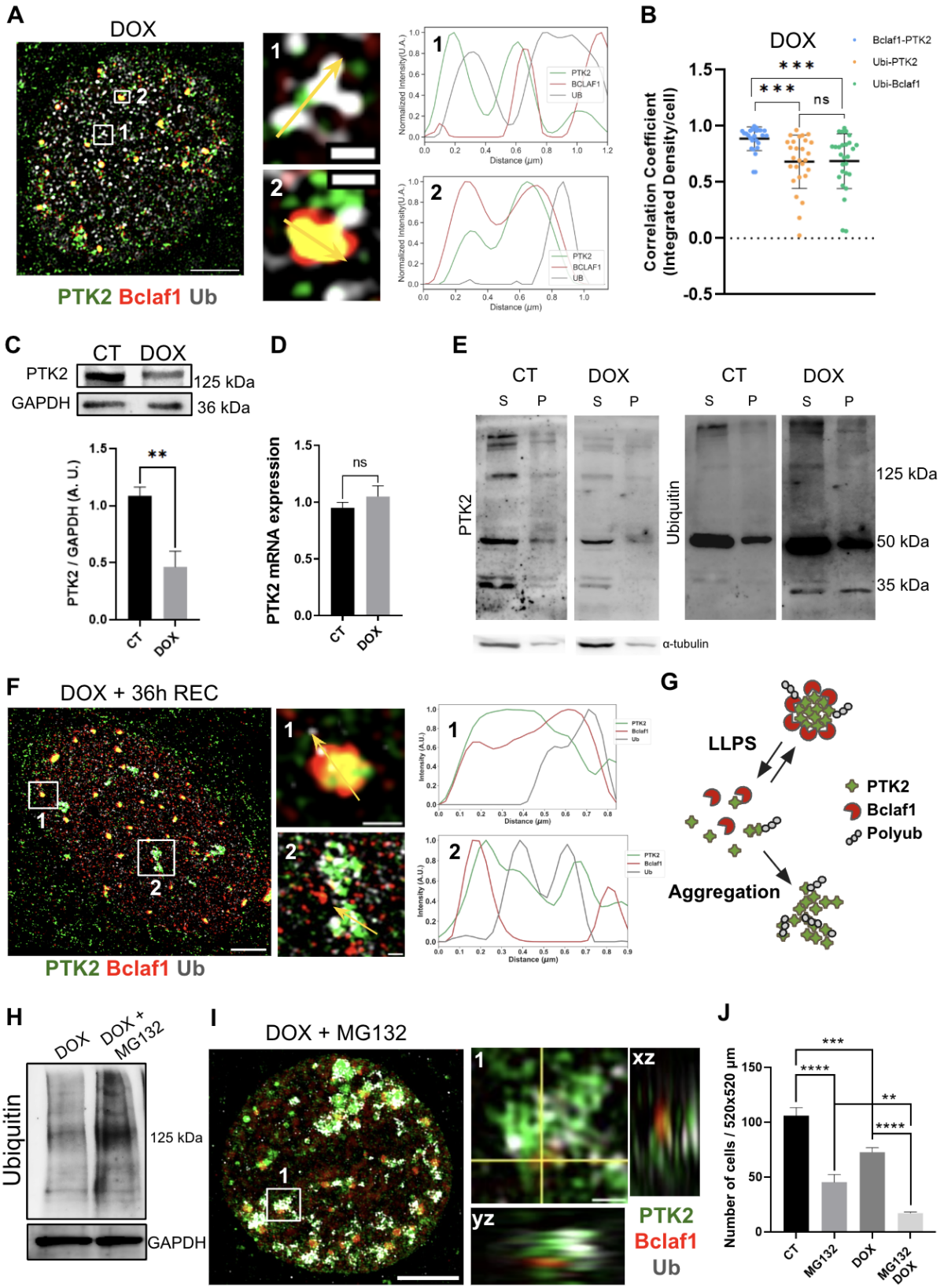

Figure 7. Bclaf1 biomolecular condensates protect PTK2 from UPS-mediated ubiquitination. A. Triple-label SR-SIM image showing PTK2 and Bclaf1 concentrated on biomolecular condensates on the nucleus of H9c2 cardiomyocytes treated with dox. Scale bar = 10 µm. **1.** Fluorescence line profile plot showing PTK2 colocalizing with ubiquitin outside the Bclaf1 condensate. Scale bar = 0.5 µm. **2.** Fluorescence line profile plot showing low

394 ubiquitin level inside the Bclaf1 condensate, where PTK2 is enriched. Scale bar = 0.5 µm **B.**
395 Pearson correlation coefficient between Bclaf1 and PTK2, ubiquitin and PTK2, and ubiquitin
396 and Bclaf1. **C.** PTK2 immunoblots of extracts from control (CT) and dox-treated (DOX) H9c2
397 cells and bar graph showing a decrease in PTK2 levels after dox treatment. **D.** RT-qPCR assay
398 shows no difference in PTK2 mRNA levels in cardiomyocytes on basal conditions or after dox
399 treatment. GAPDH was used as endogenous control. **E.** Western-blot of PTK2 and ubiquitin
400 comparing soluble (S) and insoluble (P) fractions of H9c2 cardiomyocytes. **F.** Super-resolution
401 images of PTK2, Bclaf1, and ubiquitin staining after 36 hours of recovery from dox treatment.
402 Scale bar = 5 µm. 1. Fluorescence line profile plot showing low PTK2 ubiquitination inside
403 Bclaf1 condensate. Scale bar = 0.5 µm. 2. Fluorescence line profile plot showing PTK2
404 ubiquitinated and agglomerated outside Bclaf1 condensate. **G.** Graphical representation of
405 PTK2-Bclaf1 undergoing LLPT to avoid PTK2 ubiquitination and aggregation. **H.** Western-
406 blot showing ubiquitin accumulation on cardiomyocytes treated with dox and co-treated with
407 dox and MG132. **I.** SR-SIM image showing the accumulation of ubiquitinated PTK2 on the
408 nucleus of cardiomyocytes co-treated with dox and MG132. Scale bar of nuclear image = 5
409 µm. **(1)** Orthogonal Z projection showing yz planes and xz planes of a PTK2 agglomerate,
410 which colocalize with ubiquitin. Scale bar = 0.5 µm. **J.** Cell number count after dox combined
411 with MG132 treatment, as indicated. Green: PTK2; Red: Bclaf1; Grey: Ubiquitin. Asterisks
412 demonstrates statistical significance, while ns means $P > 0.05$; * means $P \leq 0.05$; ** means P
413 ≤ 0.01; *** means $P \leq 0.001$ and **** means $P \leq 0.0001$.

414 Our SR-SIM data reveal that disrupting proteostasis through proteasome inhibition results in
415 significant PTK2 ubiquitination and accumulation in nuclear amorphous aggregates, further
416 supporting the role of the UPS in regulating PTK2 degradation. On the other hand, previous
417 studies had not yet demonstrated a ubiquitination site on PTK2 structure. To verify whether
418 PTK2 is directly ubiquitinated, we performed Co-IP coupled to mass spectrometry using H9c2
419 cardiomyocyte extracts. This approach enabled us to identify a ubiquitination site of PTK2
420 located on lysine 926 residue (Fig. 8A). In agreement with our findings, the Phosphosite
421 Platform predicts that the peptide containing the K926 residue is a potential target for
422 ubiquitination[38] (Supplem. Fig. 6). This residue is located at the beginning of the FAT domain,
423 as shown in the linear representations of PTK2-Rat and PTK2-Human (Fig. 8B). Notably, the
424 PTK2 amino acid sequence is highly conserved between rats and humans (Supplem. Fig. 6B),
425 with K926 in rats being equivalent to the K923 residue in humans. The K926 site can be
426 accessed on the FAT-PTK2 structure (Fig. 8C), making it a potential target for ubiquitin ligase
427 complexes. Furthermore, the predicted PTK2-Bclaf1 interaction model indicates that Bclaf1
428 may prevent ubiquitination of K926 by sterically occluding this site (Fig. 8D). Together, our
429 findings confirm PTK2 as a target of the UPS, underscoring the role of the UPS in regulating
430 PTK2 proteostasis during dox-induced OS. Moreover, the sequestration of PTK2 by Bclaf1
431 biomolecular condensates represents a higher-level regulatory mechanism that modulates the
432 activity of the UPS on the degradation of the pro-survival kinase PTK2 during stress conditions.

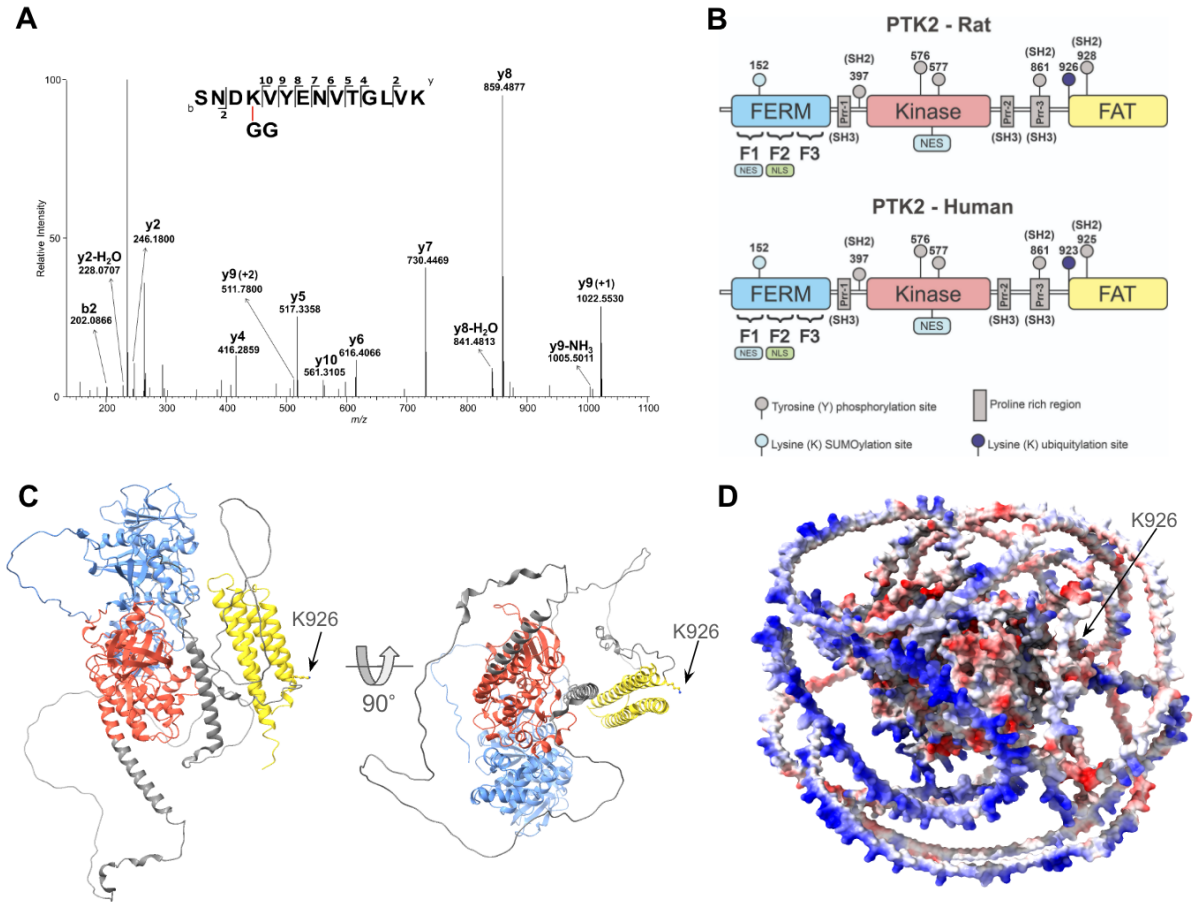

Figure 8. PTK2 is ubiquitinated on lysine 926 residue. A. MS/MS spectrum showing the PTK2 identified peptide (m/z 561.3040) with the chemical modification (K-GG) characteristic of ubiquitination. **B.** Linear representation of rat and human PTK2 demonstrating their domains and the PTK2 ubiquitination site on rat, lysine 926, and in human, lysine 923. **C.** Cartoon representation of PTK2 showing the K926 ubiquitination site on the FAT domain. **D.** Hydrostatic representation of PTK2-Bclaf1 interaction complex, showing K926 site being sterically occluded by Bclaf1. The FERM domain is represented in blue, the Kinase in red, and the FAT domain in yellow.

2.7 Bclaf1 biomolecular condensates regulate PTK2 stability to enhance cell survival

To confirm the role of Bclaf1 on PTK2 stabilization on the nucleus of cardiomyocytes during dox-induced oxidative damage, shRNA-gene knockdown and super-resolution microscopy experiments were performed. Gene knockdown (KD-Bclaf1) was confirmed by western blotting experiments (Fig. 9A; Supplem. Fig. 7F). Surprisingly, KD-Bclaf1 cells treated with dox presented an expressive protein ubiquitination, accessed by western blotting, in relation to dox-treated control cells (CT) (Fig. 9B). The increased level of protein ubiquitination after Bclaf1 depletion was confirmed by SR-SIM analysis (Fig. 9C). As expected, in KD-Bclaf1 dox-treated cells, the Bclaf1 transition to liquid phase was disrupted (Fig. 9D). Moreover, nuclear PTK2 becomes organized into amorphous aggregates colocalizing with ubiquitin

452 staining, suggesting protein destabilization and ubiquitination due to the absence of Bclaf1
453 biomolecular condensates during dox-induced OS (Fig. 9E). To confirm whether PTK2 would
454 be destabilized and tagged to UPS degradation in dox-treated KD-Bclaf1 cells, we analyzed
455 PTK2 expression by western blot and RT-qPCR. Our data showed a reduction of PTK2 protein
456 levels in KD-Bclaf1 dox-treated cells (Fig 9F; Supplem. Fig. 7G). In contrast, PTK2 mRNA
457 levels were increased (Fig. 9F), suggesting an increase in PTK2 degradation and an activation
458 of a transcriptional response trying to keep the basal levels of PTK2. The reduction of PTK2
459 levels can be attributed to the absence of Bclaf1 condensates protecting this kinase from the
460 UPS. These data sustained a molecular mechanism in which Bclaf1 biomolecular condensates
461 sequesters and protects PTK2 from oxidative damage, preventing its destabilization and UPS
462 degradation during dox treatment.

463 Supporting the role of Bclaf1 on PTK2 stabilization, Bclaf1 loss-of-function reduced soluble
464 PTK2-FL and increased its fragmentation after dox treatment (Fig. 9G). Analysis of the
465 insoluble fractions demonstrated no alterations on PTK2 bands pattern after Bclaf1 knockdown
466 (Fig. 9H). These results corroborated our previous data demonstrating PTK2 fragments are
467 primarily soluble and accessible for ubiquitination and degradation by the UPS. Furthermore,
468 our data confirm Bclaf1 as a stabilizing protein that works, via LLPS, protecting its client
469 proteins from the ubiquitination and degradation on cells under stress.

470 Given the well-established pro-survival role of PTK2[6,12,13,39], we examined whether the
471 degradation of PTK2 following Bclaf1 knockdown would affect cell survival. Our data
472 demonstrated an accumulation of p53 and PUMA, pro-apoptotic proteins, on dox-treated KD-
473 Bclaf1 cardiomyocytes (Fig. 9I; Supplem. Fig. 7H), indicating the activation of cell death by
474 apoptosis. Finally, to verify the percentage of cell death on dox-treated KD-Bclaf1 cells,
475 panoramic images were obtained to count the number of adhered cells in each field. The dox
476 treatment was done after cells reach 80% of confluence and the analysis confirms the reduction
477 of approximately 40% on cell number after 12 h of dox treatment in KD-Bclaf1 cells in relation
478 to CT cells. These data link the stabilization of PTK2 by Bclaf1 condensates with the cell's
479 ability to resist dox-induced OS. Taken together, data obtained from Bclaf1 knockdown and
480 proteasome inhibition revealed a new molecular mechanism whereby Bclaf1 biomolecular
481 condensates stabilize and protect PTK2 from ubiquitination and degradation by the ubiquitin-
482 proteasome system during dox-induced OS in cardiomyocytes, promoting cell survival.

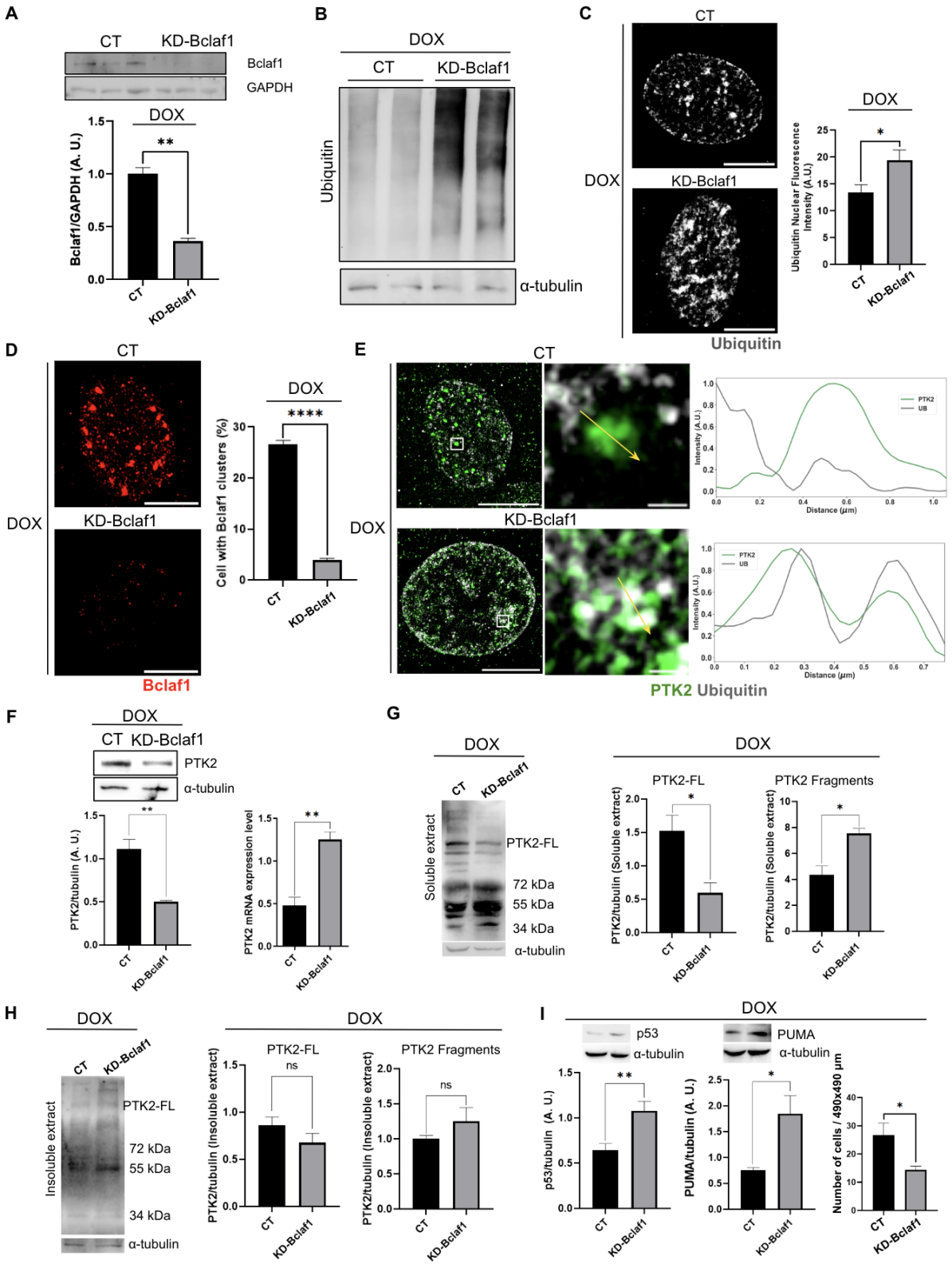

Figure 9. Bclaf1 knockdown results in PTK2 degradation and apoptosis activation. A. Western blot image and bar graph confirming the knockdown of Bclaf1 (KD-Bclaf1) in relation to control (CT) H9c2 cardiomyocytes. **B.** Western blotting images show the increased ubiquitination after Bclaf1 knockdown in relation to control cardiomyocytes, both treated with dox. **C.** SR-SIM image and bar graph show the ubiquitin accumulation on the nucleus of KD-Bclaf1 cardiomyocytes treated with dox. Scale bar = 5 μm. **D.** SR-SIM image shows the effect

of Bclaf1 knockdown on disrupting condensates assembly. Scale bar = 5 µm. **E.** SR-SIM image and line profile plot showing Bclaf1 knockdown increases PTK2 agglomeration and ubiquitination on the nucleus. Scale bar = 5 µm. Scale Bar of zoomed image = 0.5 µm. 1. Fluorescence line profile plot showing low PTK2 ubiquitination in PTK2 condensate. 2. Fluorescence line profile plot showing PTK2 ubiquitinated outside the PTK2 condensate. **F.** Western Blot and bar graphs show PTK2 levels reduction on KD-Bclaf1 cells treated with dox, while PTK2 mRNA expression levels increased. **G.** Western blot of soluble extracts from control and KD-Bclaf1 H9c2 cells treated with dox. Bar graphs show a reduction of PTK2-Full length (PTK2-FL) band and an increase in PTK2 cleaved bands (55 KDa and 34 kDa). **H.** Western blot and bar graph analysis of insoluble extract from control and KD-Bclaf1 H9c2 cells treated with dox. The analysis showed no difference between CT and KD-Bclaf1 cells on the amount of PTK2-FL and PTK2 fragments present on the insoluble fraction. **I.** Western blot and bar graphs show increased p53 and PUMA levels on KD-Bclaf1 H9c2 cardiomyocytes treated with dox. On the right, the bar graph shows a reduced number of cells on the KD-Bclaf1 cells in relation to control cells, after dox treatment.

3. DISCUSSION

Using a multi-faceted approach, we identified nuclear Bclaf1 biomolecular condensates being crucial for sequestering and protecting PTK2 from ubiquitin-proteasome-mediated degradation during dox-induced oxidative stress within submicron-scale membraneless organelles formed by LLPS. Disrupting Bclaf1 condensates led to increased PTK2 ubiquitination and degradation, ultimately activating cell death via apoptotic pathways. We also identified a specific lysine ubiquitination site on PTK2, providing the first experimental evidence for the involvement of the ubiquitin-proteasome system in regulating PTK2 levels in cardiomyocytes. Furthermore, our findings establish Bclaf1 biomolecular condensates as nuclear sites that counteracts the activity of the ubiquitin-proteasome system over PTK2 during dox-induced OS. We highlight a novel protein quality-control mechanism for PTK2 during oxidative stress, demonstrating how Bclaf1 stabilizes proteins to modulate cell survival.

An important aspect of our Co-IP coupled to MS/MS data was the use of a PTK2 Flag-FERM-domain as a bait to identify new PTK2 interactors prone to stabilize PTK2 during stress. Consequently, PTK2 FERM domain is enough to mediate its interaction with Bclaf1, an essential process to enhance cell survival during OS. The PTK2 FERM mediates protein-protein interactions that are necessary for PTK2 function in the nuclear subcompartment[1]. In the nucleus, PTK2-FERM domain interacts with and regulates the levels of transcription factors, including p53 and GATA4[6]. FERM forms a complex with p53 and MDM2, an ubiquitin ligase family member, bringing these proteins into close proximity and facilitating p53 ubiquitination and degradation via UPS, ultimately promoting cell survival[12]. In this study, we describe a novel pro-survival mechanism whereby PTK2 is stabilized and protected from

527 UPS-mediated degradation by Bclaf1 condensates during OS. The maintenance of functional
528 PTK2 may consequently support its p53-MDM2 regulatory pro-survival mechanism. Although
529 the search for new nuclear interacting partners for PTK2 FERM-domain has been increasing,
530 FERM mediating Bclaf1 interaction was described for the first time and adds a new layer of
531 information on pro-survival mechanisms activated during stress.

532 Corroborating the responsiveness of PTK2 to different kinds of stimuli[2,4,8,40], we demonstrated
533 that PTK2 accumulates in the nucleus of cardiomyocytes under OS. Moreover, our data
534 demonstrated that dox-induced OS led to the phosphorylation of tyrosine 397 of PTK2, a
535 necessary event for PTK2 activation (Fig. 2C, F). Inactive PTK2 is found in an auto-inhibited
536 conformation, with FERM binding to the Kinase domain, physically inhibiting its activation[21].
537 PTK2 activation requires dimerization, concomitantly with the binding of the FERM domain
538 to phosphatidylinositol-4,5-biphosphate, allowing PTK2 Y397 autophosphorylation and
539 activation[41]. Then, in the open conformation, binding sites are exposed to modulate signaling
540 pathways through protein-protein interactions[41–43]. The responsiveness of PTK2 to dox-
541 induced oxidative and, consequently, genotoxic stress accumulating in the nucleus of
542 cardiomyocytes may be linked with its role in regulating p53 levels[6,12]. Indeed, when PTK2
543 levels were reduced after Bclaf1 knockdown, we observed increased p53 levels (Fig. 9I),
544 ultimately resulting in apoptosis. In line with our findings, previous studies in mice have
545 demonstrated that PTK2 protects the heart during dox treatment by maintaining appropriate
546 p21 levels to promote cell survival[13].

547 Using super-resolution microscopy and FRAP approaches, we demonstrated that PTK2
548 localizes within Bclaf1 biomolecular condensates in dox-treated cardiomyocytes (Fig. 3),
549 supporting previous findings on condensate formation in response to stress[28,29,44]. Biomolecular
550 condensates are membraneless compartments in which protein can be sequestered, modified,
551 and stabilized[45–47]. Previous studies demonstrated Bclaf1 interacting with and stabilizing HIF1-
552 α and PD-L1 by modulating their ubiquitination levels during hypoxia and after irradiation,
553 respectively, although the underlying mechanisms remain poorly understood[16,17,48].
554 Nevertheless, no studies have examined the potential role of Bclaf1 in stabilizing proteins
555 through LLPS during stress. Here, we propose an overall mechanism by which Bclaf1, through
556 liquid-liquid phase separation, counteracts the ubiquitin-proteasome system, stabilizing
557 proteins involved in adaptive stress responses and ultimately modulating cell fate. Bclaf1 is an
558 intrinsically disordered protein[49], whereas PTK2 contains two intrinsically disordered regions

559 (Fig. 4E). Our analysis suggests that Bclaf1 primarily undergoes LLPS forming nuclear
560 biomolecular condensates. On the other hand, the interaction of Bclaf1 with the PTK2 IDRs
561 may induce PTK2 phase transition and translocation into the membraneless organelles, where
562 this kinase is stabilized and protected from the UPS. FRAP experiments revealed enhanced
563 mobility for both proteins within the condensates, with Bclaf1 exhibiting higher mobility (Fig.
564 5A). FLIM results demonstrated increased fluorescence lifetimes in both Bclaf1 and PTK2
565 condensates (Figure 5C), likely due to the increased concentration of these proteins within
566 these structures. These findings align with previous observations in other membraneless
567 organelles, including speckles, stress granules, and the nucleolus[50]. Interestingly, previous
568 studies demonstrated that PTK2 undergoes LLPS in focal adhesions in the presence of paxillin.
569 The droplet formation was linked to PTK2 oligomerization, facilitated by the interaction
570 between FERM-FERM and FERM-FAT domains, which promoted the formation of liquid
571 condensates[50,51].

572 Studies have demonstrated that molecular chaperones may regulate the biomolecular
573 condensates phisiology[29]. Chaperones are essential proteins that actively remodel protein-
574 protein interactions and facilitate protein folding[52,53]. While their role in maintaining protein
575 quality and preventing aggregation is well-established, the emerging field of biomolecular
576 condensates is revealing their function in regulating the material properties and functions. For
577 instance, disaggregases chaperones, including Hsp70 and AAA+ATPases, can modify the
578 porosity of condensates, facilitating a quicker exchange of materials with the surrounding
579 environment[29,54]. Chaperones can also have a role in condensate assembly or disassembly[28]. In
580 this context, using FRAP experiments combined with Hsp70 inhibition, we confirmed the
581 impact of Hsp70 activity on the Bclaf1 mobility into early formed biomolecular condensates
582 (Fig. 6A-B). Some studies exploring Hsp70 role on condensate dynamics suggest an action for
583 this chaperone on the quality control and maintenance of the condensates[55], while others
584 suggest chaperones can act on the disassembly of the condensates, removing proteins during
585 stress recovery[37]. Our data indicates a role of Hsp70 on the dynamics of Bclaf1 condensates,
586 possibly restructuring their components to ensure their continued activity during dox-induced
587 OS.

588 Oxidative stress generated by dox is a primary cause of cardiotoxicity[56]. The overproduction
589 of ROS induces oxidative damage to biological macromolecules, including proteins, lipids, and
590 DNA, and can induce cardiomyocyte apoptosis[57,58]. Proteins are the primary targets of

591 oxidative modifications, which induces conformational changes and the exposure of internal
592 regions to the solvent, resulting in protein ubiquitination. Oxidatively modified proteins must
593 be degraded by the proteasome system to maintain cellular proteostasis and, ultimately, cell
594 survival[59,60]. Our data revealed a progressive increase in OS from 1 to 6 hours of dox treatment,
595 reaching a peak at 6 hours. This coincided with the nuclear accumulation of Bclaf1
596 biomolecular condensates, suggesting Bclaf1 LLPS is a response to elevated ROS levels (Fig.
597 6C-G). Additionally, cell viability remained preserved up to 6 hours of treatment, indicating
598 that LLPS plays a role in enhancing cell survival during OS. Next, in line with the effects of
599 dox in the oxidation and ubiquitination of proteins, we demonstrated that PTK2 is susceptible
600 to the effects of oxidative damage being fragmented and targeted by the UPS after dox
601 treatment (Fig. 7). Analysis of soluble and insoluble fractions confirmed the propensity of
602 PTK2 to remain in the soluble fraction, prone to be degraded by proteasomes after 12 hours of
603 dox treatment. Otherwise, ubiquitinated PTK2 can aggregate in the nucleus of cardiomyocytes
604 exposed to 48 hours of OS. Furthermore, PTK2 sequestered into the Bclaf1 condensates
605 becomes less accessible to be ubiquitinated and consequently degraded by proteasomes. These
606 findings corroborate the previous function described for Bclaf1 in the stabilization of HIF-1a
607 during hypoxia[17].

608 The regulation of PTK2 homeostasis by ubiquitination and proteasome degradation has been
609 previously investigated[61,62], however, as far as we know, there is no literature describing in
610 which specific sites PTK2 is ubiquitinated or confirming its proteolytic degradation by
611 proteasomes. Our co-immunoprecipitation assay coupled to mass spectrometry identified K926
612 as a target for ubiquitin-ligases (Fig. 8), a complex that recognizes and transfers a ubiquitin
613 chain to lysine residues exposed in the surface of proteins containing degradations signals[63,64].
614 Next, we confirmed the UPS action on PTK2 homeostasis performing the pharmacological
615 inhibition of proteasomes. The accumulation of ubiquitinated PTK2 in the nucleus, as revealed
616 by super-resolution microscopy, provided strong evidence for the ubiquitin-proteasome system
617 as a key regulator of nuclear PTK2 degradation (Fig. 7). Our findings on PTK2 quality control
618 suggest a dynamic mobility of PTK2 within Bclaf1 biomolecular condensates, where this
619 kinase is protected from UPS-mediated degradation. However, PTK2 diffused throughout the
620 nucleus can be destabilized by oxidative damage, leading to its ubiquitination and proteasome
621 degradation or to its accumulation in amorphous nuclear aggregates after an extended
622 exposition to OS.

623 PTK2 regulates distinct cellular functions in cardiomyocytes, including survival during stress
624 conditions[1,2,4,39]. Here, we present strong evidence that Bclaf1 condensates protect PTK2
625 against the UPS in a crucial mechanism for enhanced cardiomyocyte survival during OS. For
626 note, Bclaf1 knockdown resulted in increased general protein ubiquitination, including PTK2,
627 pointing towards a broad role for Bclaf1 in counteracting the UPS on proteostasis control
628 during stress (Fig. 9)[12,65]. Furthermore, we observed reduced PTK2 levels and an accumulation
629 of p53 following Bclaf1 knockdown, ultimately leading to cell death via the activation of
630 apoptotic pathways (Fig. 9). It is plausible that the reduction of PTK2 availability contributes
631 to p53 accumulation and subsequent apoptosis activation. Previous studies have demonstrated
632 a role of αβ-crystallin to protect PTK2 from cytoplasmic calpain mediated-degradation in
633 cardiomyocytes under mechanical stress, allowing cells to survive[4]. Here, we present evidence
634 that Bclaf1 condensates play a similar role stabilizing nuclear PTK2 during OS. Indeed, past
635 research demonstrated Bclaf1 knockout sensitized cells to TNF induced apoptosis, suggesting
636 a regulatory role for this protein on cell fate[66].

637 Our findings strongly support the role of Bclaf1 biomolecular condensates in counteracting
638 PTK2 degradation by the ubiquitin-proteasome system, thereby regulating PTK2 homeostasis
639 to promote cardiomyocyte survival during doxorubicin-induced oxidative stress and
640 cytotoxicity.

641 **4. MATERIAL AND METHODS**

642 **4.1 Cell culture**

643 H9c2 cardiomyocytes, derived from rat embryos ventricular myoblasts, were obtained from
644 American Type Culture Collection (ATCC). Cells were cultured in high-glucose DMEM
645 supplemented with 3.7 g/L sodium bicarbonate, 10% FBS, and 1% penicillin/streptomycin
646 solution (Sigma-Aldrich, P0781) at 37 °C with 5% CO_2 atmosphere in a humidified incubator.
647 Medium was changed every 2 days, and cells were trypsinized (Trypsin-EDTA) and split as
648 soon as they reached around 70% confluence. Cells were counted using a Neubauer chamber
649 to determine the appropriate seeding densities for each experiment.

650 **4.2 Cell treatments**

651 **Doxorubicin:** Doxorubicin powder was dissolved on water at 2 mg/mL. Then, for H9c2
652 cardiomyocytes treatments, dox was diluted on the complete medium (DMEM) with FBS and

653 antibiotic in a final concentration of 1 μM. For recovery experiments, cells were treated with
654 dox (1 μM) for 3 or 12 hours and then were incubated in complete medium for 12 and 36 hours.
655 The other experiments were performed after 12 hours of dox treatment.

656 **MG132:** MG132 proteasome inhibitor (Sigma, M7449) was diluted on complete DMEM
657 medium at 5 μM and cells were treated, in combination with dox (1 μM), for 12 hours. Control
658 cells were treated with DMSO (vehicle) at the same volume as the proteasome inhibitor. After
659 12 hours, cells were fixed, or samples were extracted.

660 **VER-155008:** VER-155008 Hsp70 inhibitor (Sigma, SML0271) was diluted with DMSO as a
661 stock solution at 5 mM and used at a final concentration of 50 μM[67]. Cells were treated for 3 h
662 with dox (1 μM) followed by 1h of the Hsp70 inhibitor. For the experiments, the medium was
663 changed to DMEM with FBS and antibiotics.

664 **4.3 Coimmunoprecipitation assays**

665 Proteins were extracted from H9c2 cells using Pierce™ Classic IP Kit (Thermo Fisher, 26146)
666 with lysis buffer and protease inhibitor cocktail with EDTA on ice. Cells were lysed for 5
667 minutes using a cell scraper. Each sample was collected, agitated on a vortex, and stored in ice
668 for 15 min. Next, samples were centrifuged to 12000 RPM for 20 minutes at 4ºC. The pellet
669 was discarded, and the supernatant was stored at -20ºC for the co-immunoprecipitation assays.
670 Protein quantification was performed using the BCA Protein Assay Kit (Thermo Fisher,
671 23225). Equal amounts of total extracts were used for co-immunoprecipitation using specific
672 antibodies against PTK2 and Bclaf1 according to the manufacturer's instruction.

673 **4.4 Western blotting**

674 H9c2 cells were lysed for 5 minutes using a RIPA buffer on ice, using a cell scraper. Each
675 sample was collected, agitated on a vortex, and stored in ice for 15 min. Then, samples were
676 centrifuged to 12000 RPM for 20 minutes at 4ºC. The pellet was discarded, and the supernatant
677 was quantified using Pierce BSA Assay Kit (Thermo Fisher, A55864) and then diluted on a 2X
678 Laemmli loading buffer with β-mercaptoethanol. Next, samples were separated on 6%, 8%, or
679 12% SDS-polyacrylamide gels using prestained PageRuler (SM0761, Fermentas) as protein
680 ladder. Proteins were transferred from gels to PVDF membranes, which were blocked with 5%
681 BSA-TBS-T solution under agitation for 40 minutes. Then, the membranes were washed with
682 TBS-T once and incubated with primary antibodies against PTK2 (Thermo Fisher, AHO0502),

683 pPTK2 (Thermo Fisher, GTX50185), Bclaf1 (Thermo Fisher, PA578299), p53 (Thermo
684 Fisher, MA1-7629), p-p53 (Thermo Fisher, PA5-117179), cleaved caspase-3 (Thermo Fisher,
685 PA5114687), ubiquitin (Thermo Fisher, 13-1600), PUMA (Thermo Fisher, MA531994),
686 GAPDH (SC-25778), α-tubulin (Sigma, T9026) and histone H1 (Thermo Fisher, PA5-30055)
687 overnight. The dilution used for primary antibodies was 1µg/mL in 3% BSA-TBS-T solution.
688 Next, the membranes were washed 3 times (10 minutes) with TBS-T and incubated with
689 peroxidase conjugated secondary antibodies Goat Anti-Rabbit IgG (H + L)-HRP Conjugate
690 (Bio-Rad, 1706515) or Goat Anti-Mouse IgG (H + L)-HRP Conjugate (Bio-Rad, 1706516) in
691 3% BSA-TBS-T solution for 1 hour and 30 minutes under mild agitation. After the incubation,
692 membranes were washed 3 times (10 minutes) with TBS-T and visualized using the Clarity
693 Western ECL Blotting Substrate (Bio-Rad, 1705060) in a Uvitec Documentation System.

694 **4.5 Nuclear and Cytoplasmic Extraction**

695 H9c2 cells were trypsinized and the nuclear and cytoplasmic protein extracts were obtained
696 using NE-PER Nuclear and Cytoplasmic Extraction Reagents (Thermo Fisher, 78833),
697 following the fabricant instructions.

698 **4.6 Soluble and insoluble extraction**

699 Proteins were extracted from H9c2 cells using Tris-saline solution (Tris-HCl: 50 mmol/L,
700 NaCl: 150 mmol/L; pH: 7,6) containing protease inhibitor cocktail with EDTA on ice. Cells
701 were scraped off the plates using a cell scraper, followed by sonication for 15 seconds, repeated
702 for three times. The samples were then centrifuged at 12000 RPM for 30 minutes at 4ºC and
703 the supernatant was separated from the pellet. The pellet was solubilized in a solution of urea
704 6 M; SDS 2%; Tris-base 50 mM (pH 7,5); DTT 50 mM and incubated in a dry bath for 15 min
705 at 60°C. Next, 5X Laemmli loading buffer with β-mercaptoethanol was added to all samples,
706 followed by incubation in a dry bath for 5 minutes at 95°C. Finally, the samples were stored at
707 -20ºC.

708 **4.7 Immunofluorescence**

709 H9c2 cells were counted and seeded on 24 well plates containing coverslip (ThorLabs,
710 0117520). An amount of $2x10^4$ cells were plated for well, which were maintained in high
711 glucose DMEM supplemented with 3.7 g/L sodium bicarbonate, 10% FBS and 1%
712 penicillin/streptomycin solution. After cell adhesion to the coverslip, the treatments were

713 conducted as described above. Then, cells were fixed using 4% paraformaldehyde, blocked and
714 permeabilized using a solution with 3% bovine serum albumin and 0.1 % Triton-X in 0.1 mol/L
715 DPBS on ice. Samples were incubated with primary antibodies against Bclaf1 (Thermo Fisher,
716 PA5-78299 - 1:200 or Thermo Fisher, PA5-78299 - 1:200) and ubiquitin (Thermo Fisher, 13-
717 600 - 1:100) for 30 minutes at room temperature. Other combinations were performed with
718 antibodies against phosphorylated PTK2 (Thermo Fisher, 44-625G - 1:200) and Hsp70
719 (Thermo Fisher, MA3-006 - 1:50). Next, after rinsing, cells were labeled with Alexa Fluor-
720 546-conjugated goat anti-rabbit (Thermo Fisher, A-11010 - 1:2000), Alexa Fluor-647-
721 conjugated goat anti-mouse (Thermo Fisher, A-21235 - 1:2000) for 30 minutes at room
722 temperature. Then, cells were labeled using FAK Monoclonal Antibody Alexa Fluor-488
723 (Thermo Fisher, MA3-96500-A488 - 1:200) for 30 minutes at room temperature. When the
724 actin cytoskeleton was stained, Phalloidin-Alexa Fluor 647 was used (Thermo Fisher, A22287
725 - 1:40). After each incubation, the excess of antibodies was removed, washing 3 times using 1
726 mL of DPBS per well and agitating the plate on an orbital shaker for 5 minutes. Slides were
727 mounted using ProLong Gold Antifade Mountant with DAPI.

728 **4.8 Proximity Ligation Assay**

729 H9c2 cells were plated on glass slides and fixed with 10% buffered formalin. Next, samples
730 were incubated with glycine 100 mM and blocked using Duolink Blocking Solution (Sigma,
731 DUO82007). Then, primary antibodies against PTK2 (Thermo Fisher, ZF002, mouse) and
732 Bclaf1 (Thermo Fisher, PA5-78299, rabbit) were added to a 1:200 concentration and incubated
733 in a humidity chamber at 4ºC for 1 hour. The excess of antibodies was removed, and MINUS
734 (DUO92004-100RXN, Sigma) and PLUS PLA (Sigma, DUO92002-100RXN) probes were
735 added and incubated in a humidity chamber at 37ºC for 1h and 10 minutes. Next, samples were
736 incubated with ligation solution for 30 minutes at 37ºC. Finally, an amplification buffer was
737 added, and slides were incubated in a humidity chamber for 100 minutes at 37ºC. After each
738 step, samples were washed for 5 minutes at room temperature using a wash buffer.

739 **4.9 CellROX**

740 H9c2 cells were plated on glass slides and treated with dox at 1 μM concentration during
741 different times (1h, 3h, 6h and 12h). Next, CellROX Green Reagent (Thermo Fisher, C10444)
742 was added at 5 μM concentration and incubated at 37ºC for 30 minutes on an incubator. Then,

743 cells were fixed using 4% paraformaldehyde solution and images were obtained in a confocal
744 microscope using a 488 nm laser.

745 **4.10 Transfection**

746 For the Fluorescence lifetime imaging microscopy (FLIM) and Fluorescence recovery after
747 photobleaching (FRAP) assays, cells were plated in a 35 mm glass bottom dish with 20 mm
748 microwell (Cellvis, D35C4-20-0-N) and transfected with lipofectamine reagent (Invitrogen,
749 L3000015) following the manufacturer's instructions, using a medium supplemented with 5%
750 FBS. After 1 day of transfection, the medium was replaced by a supplemented medium with
751 10% FBS for 24 hours. Then, the cells were treated with dox at 1 μM concentration for 3 hours.
752 For experiments with Hsp70 inhibitor, cells were treated for 1 hour with VER-155008 after the
753 treatment with dox. Cells were transfected with the EGFP-PTK2 or with the EGFP- Bclaf1
754 vectors (SynBio Technologies).

755 **4.11 FLIM and FRAP**

756 Experiments were performed on a LSM780-NLO Microscope (Carl Zeiss AG, Germany) using
757 the EC Plan-Neofluar 40x/1.30 Oil DIC objective. Cells were maintained at 37 C° and 5% CO2
758 during acquisition. FLIM images were acquired using a TCSPC system from Becker-Hickl -
759 Germany with a Hybrid-PMT HPM-100-40 detector. GFP fluorescence was excited at 488 nm
760 by Two-Photon Excited Fluorescence using a ChameleonDiscovery NX (Coherent - USA)
761 operating at 976 nm. In the FRAP experiments, a time series of 200 images were taken with a
762 speed of 9 frames per second up to 5 min with an imaging area of 512 pixels × 512 pixels. The
763 regions of interest were bleached down to 80% of original fluorescence signal excited by the
764 488 nm laser of the microscope. Fitting of the recovery fluorescence intensity (RFI) was done
765 using the following equation: $RFI = MF(1 - e^{(-b*t)})$. Where MF represents the mobile
766 fraction, which ranges from 0 to 1, b is a constant related to the fluorescence recovery rate, and
767 t is the time post-bleaching.

768 **4.12 MTT**

769 H9c2 cells were seeded at 1 x 10^4 per well in a 96 well plate, for the MTT assays. After
770 adhesion, cells were treated with dox during distinct times (1h, 3h, 6h and 12h). Then, the
771 medium was replaced for the MTT solution (0.5 mg/mL), and cells were maintained for 4 hours
772 at 37ºC in an incubator. After the incubation, the precipitated crystals were diluted in DMSO

773 and incubated for 10 minutes at 37ºC. Then, in a plate reader, the absorbance was measured on
774 a wavelength of 540 nm to determine cell viability. Seven replicates were done.

775 **4.13 Short Hairpin RNA-mediated gene silencing**

776 The short hairpin RNA (shRNA) sequence targeting Bclaf1 (*Rattus norvegicus*) was retrieved
777 from the Broad Institute portal (https://portals.broadinstitute.org/). We selected a sequence
778 located after 150 bp of the beginning of the coding sequence (CDS) with a GC content between
779 25% and 60% and excluding any candidate with a run of 7 C/G bases. The shRNA selected
780 (5'-TGCTACATCTGGTGATATTTG-3') was cloned into the plasmid PlKO.1 hygro
781 (Addgene, #24150) previously digested with AgeI (NEB, #R0552S) and EcoRI (NEB,
782 #R0101S) enzymes. The cloned plasmid was co-transfected with pCMV delta R8.2 (Addgene,
783 #12263), and pMD2.G (Addgene, #12259) into Lenti-X 293T Cell Line (Takara Bio) for
784 lentivirus packaging. The viral supernatant was then used to transduce H9c2 cells in the
785 presence of polybrene (8 µg/mL) (Sigma-Aldrich, H9268) for 18 hours. Five days post-
786 transduction, the selection was started using hygromycin (Thermo Fisher, Gibco 10687010) at
787 a dose of 200 µg/mL for 5 days.

788 **4.14 Microscopy analysis**

789 SR-SIM images were acquired on a Zeiss Elyra PS.1 microscope, using PlanApochromat
790 63x/1.4 Oil DIC objective in the 3D-SIM mode. 3D-SIM z-stacks were projected on a single
791 plane with summed intensities using the ImageJ-FIJI software. Correlation analysis was
792 performed following the same method described by Galiani *et al.*[68], using Bclaf1 clusters as
793 origins to draw circles and calculate the integrated density fluorescence correlation. Chromatic
794 3D correction was performed by imaging different z planes of fluorescent sub-resolution beads
795 using the same filter configuration for each channel as on the cell images. The resulting image
796 was affine transformed by Zen Software (Zeiss) using the 488 nm channel as base position.

797 **4.15 RT-qPCR**

798 Total RNA was extracted using TRIzol according to Chomczynski & Sacchi[69]. One microgram
799 was reverse transcribed using random primers and the Omniscript RT Kit (Qiagen, 205113)
800 polymerase kit. Primers were designed using Primer3 software (primer3plus.com). The primer
801 concentrations used in qPCR reactions were defined by testing different concentrations (200
802 nM, 400 nM and 800 nM). The lowest concentration without impact on product amplification

803 and dimer formation was used for the experiments. The GAPDH gene was used as an
804 endogenous control. The primers sequences are as follows: PTK2—
805 5'GAGACCATTCCCATCCTTCCA3' and 5'GTCGGAGTTCAGCAGCTTCT3' (200 nM).
806 GAPDH—5'GGAGCGAGATCCCTCCAAAAT3' and 5'GGCTGTTGTCATACTTCT
807 CATGG3' (200 nM). For qPCR reactions, we used SYBR Green PCR Kit (Quantinova,
808 208052), 50 ng of cDNA, primers (200 nM) and Milli-Q water to reach the final reaction
809 volume. Samples were assayed in triplicate and analysis was performed with a 7500 RT-PCR
810 system (Applied Biosystems, California, USA).

811 **4.16 Mass Spectrometry analysis of ubiquitinated sites**

812 Following the PTK2 immunoprecipitation, we performed on-bead protein digestion. Briefly,
813 matrix-associated proteins were resuspended in ammonium bicarbonate (AmBic 50 mM) and
814 digested using trypsin (1:50 enzyme-to-substrate ratio) overnight at 36°C. Peptides were
815 acidified with 0.1% formic acid and 2 µg of the mixture was loaded onto an Ultimate 3000
816 system (Thermo Scientific) coupled to an Orbitrap Exploris 240 (Thermo Scientific). Peptides
817 were separated using an Acclaim PepMap RSLC C18 column (Thermo Scientific) with a binary
818 gradient of acetonitrile (ACN) in 0.1% formic acid (FA). The gradient increased from 1% to
819 40% ACN over 120 minutes. For mass spectrometry analysis, data-dependent acquisition
820 (DDA) was employed, with Precursor ions being analyzed with a resolution of 60,000. The top
821 20 most intense ions with charges of 2+ and 3+ were selected for MS/MS fragmentation using
822 normalized collision energy (NCE) of 25, 30, and 35. Additionally, MS/MS spectra were
823 acquired at a resolution of 15,000 with a dynamic exclusion time of 10 seconds. LC-MS raw
824 data were analyzed using PatternLab V software[70]. Peptide spectral match was carried out
825 against the *Rattus norvegicus* protein database from UniProt (version: 2023_02). Search
826 parameters included -GG variable modification (m/z = 114.042927) in lysines and n-terminus
827 to search ubiquitination sites.

828 **4.17 Structural predictions**

829 Protein sequences were obtained from UniProt, and their structures and potential interaction
830 models were predicted using AlphaFold-Multimer[24,25,25]. This specialized version of
831 AlphaFold was used to predict both individual protein structures and protein complexes
832 models. The accuracy of the predicted complex structures was assessed using the pTM score,
833 with scores above 0.5 indicating potential similarity to the true structures. However, pTM

834 scores should be interpreted cautiously, as they can be influenced by the accuracy of individual
835 protein components. To visualize and analyze the predicted structures, we employed UCSF
836 ChimeraX, which allowed us to create 3D models and align different AlphaFold-predicted
837 models to select the most representative structure[24]. To evaluate the propensity of the proteins
838 to form biomolecular condensates, we utilized liquid-liquid phase separation (LLPS) prediction
839 software including FuzDrop and PSPredictor. The FuzDrop server has four main application
840 areas related to condensed states: (i) proteins are analyzed for liquid-liquid phase separation
841 (LLPS) by calculating their droplet formation probability (pLLPS), with a threshold of 0.60
842 indicating a high likelihood of driving droplet formation; (ii) protein regions that promote
843 droplet formation are identified, focusing on those with a droplet-promoting probability (pDP)
844 ≥ 0.60 and at least 10 residues; (iii) droplet-client proteins, which cannot spontaneously
845 undergo LLPS but contain droplet-promoting regions, are also identified, as they can partition
846 into droplets through interactions with other protein; (iv) and aggregation hot-spots within
847 droplets are detected by combining predictions on droplet-promoting regions with interaction
848 diversity data using FuzPred[30]. Additionally, we used PSPredictor, a machine learning-based
849 tool that predicts propensity of proteins undergoing phase separation. LLPS propensity scores
850 above 0.60 were considered indicative of a high probability for condensate formation.
851 PSPredictor employs sophisticated algorithms and a curated database of phase-separating
852 proteins to provide accurate LLPS predictions[71].

853 **4.18 Statistical analysis**

854 Statistical analysis was performed on GraphPad Prism software using Shapiro-Wilk and
855 Kolmogorov-Smirnov tests for normality of the sample distribution and ANOVA or Mann-
856 Whitney U tests for the analysis of variance between samples. P values < 0.05 were considered
857 statistically significant, while * means P ≤ 0.05, ** means P ≤ 0.01, *** means P ≤ 0.001 and
858 **** means P ≤ 0.0001.

AUTHOR CONTRIBUTIONS

Conceptualization and methodology: AMS, AAT, IAM, and BRIR. Cell culture, treatments and sample extraction: IAM, BRIR, AGA, APS, PVCC, MGSC, and AMS; Differentiation assays: LBN and AMS. Super-resolution microscopy experiments and data analysis: IAM, BRIR, MCS, IRB, LBN, AMS and AAT; FRAP and FLIM: BRIR, IAM, AMS and AAT; PLA assays, imaging and data analysis: FLB, IAM and JK; RT-qPCR: IAM and MVG; PTK2 primers design: MVG; Mass spectrometry and data analysis: GLA, GRO, PCC, MDMS, RD, AGA, IAM, AMS and FCG; Short hairpin RNA sequences design: CHGS; Short hairpin RNA-mediated gene knockdown: FVR and CHGS; Biological interpretation: IAM, BRIR, HFC, AAT, and AMS; Writing: IAM, BRIR, HFC, AAT, and AMS. All authors edited and revised the final version of the manuscript.

ACKNOWLEDGEMENTS

We thank the access to equipment and assistance provided by the National Institute of Science and Technology on Photonics Applied to Cell Biology (INFABIC) at the State University of Campinas; INFABIC is co-funded by Fundação de Amparo à Pesquisa do Estado de São Paulo (FAPESP) (2014/50938-8) and Conselho Nacional de Desenvolvimento Científico e Tecnológico (CNPq) (465699/2014-6).

This research was supported by the Coordenação de Aperfeiçoamento de Pessoal de Nível Superior – Brasil (CAPES) (88887.513417/2020-00), the National Council for Scientific and Technological Development (CNPq) (423228/2018-8), the São Paulo Research Foundation (FAPESP) (2021/02303-7, 2018/07383-6, and 2020/11824-8) and the Fundação de Desenvolvimento da UNICAMP (FUNCAMP) (87/23-2545/23).

DATA AVAILABILITY

Proteomics data were deposited in the ProteomeXchange Consortium via the PRIDE partner repository (accession no. PXD057681).

COMPETING INTERESTS STATEMENT

The authors declare no competing interests.

892 **REFERENCES**

893 1. Frame, M. C., Patel, H., Serrels, B., Lietha, D. & Eck, M. J. The FERM domain: organizing
894 the structure and function of FAK. *Nat. Rev. Mol. Cell Biol.* **11**, 802–814 (2010).
895 2. Santos, A. M. *et al.* FERM domain interaction with myosin negatively regulates FAK in
896 cardiomyocyte hypertrophy. *Nat. Chem. Biol.* **8**, 102–110 (2012).
897 3. Fonseca, P. M. *et al.* Targeting to C-Terminal Myosin Heavy Chain May Explain
898 Mechanotransduction Involving Focal Adhesion Kinase in Cardiac Myocytes. *Circ. Res.*
899 **96**, 73–81 (2005).
900 4. Pereira, M. B. *et al.* αB-crystallin interacts with and prevents stress-activated proteolysis
901 of focal adhesion kinase by calpain in cardiomyocytes. *Nat. Commun.* **5**, 5159 (2014).
902 5. Mitra, S. K., Hanson, D. A. & Schlaepfer, D. D. Focal adhesion kinase: in command and
903 control of cell motility. *Nat. Rev. Mol. Cell Biol.* **6**, 56–68 (2005).
904 6. Zhou, J., Yi, Q. & Tang, L. The roles of nuclear focal adhesion kinase (FAK) on Cancer:
905 a focused review. *J. Exp. Clin. Cancer Res. CR* **38**, 250 (2019).
906 7. Schlaepfer, D. D., Hauck, C. R. & Sieg, D. J. Signaling through focal adhesion kinase.
907 *Prog. Biophys. Mol. Biol.* **71**, 435–478 (1999).
908 8. Marin, T. M. *et al.* Shp2 negatively regulates growth in cardiomyocytes by controlling
909 focal adhesion kinase/Src and mTOR pathways. *Circ. Res.* **103**, 813–824 (2008).
910 9. Senyo, S. E., Koshman, Y. E. & Russell, B. Stimulus interval, rate and direction
911 differentially regulate phosphorylation for mechanotransduction in neonatal cardiac
912 myocytes. *FEBS Lett.* **581**, 4241–4247 (2007).
913 10. Nadruz, W., Corat, M. A. F., Marin, T. M., Guimarães Pereira, G. A. & Franchini, K. G.
914 Focal adhesion kinase mediates MEF2 and c-Jun activation by stretch: role in the activation
915 of the cardiac hypertrophic genetic program. *Cardiovasc. Res.* **68**, 87–97 (2005).
916 11. Clemente, C. F. M. Z. *et al.* Focal adhesion kinase governs cardiac concentric hypertrophic
917 growth by activating the AKT and mTOR pathways. *J. Mol. Cell. Cardiol.* **52**, 493–501
918 (2012).
919 12. Lim, S.-T. *et al.* Nuclear FAK promotes cell proliferation and survival through FERM-
920 enhanced p53 degradation. *Mol. Cell* **29**, 9–22 (2008).
921 13. Cheng, Z. *et al.* Focal adhesion kinase antagonizes doxorubicin cardiotoxicity via
922 p21(Cip1.). *J. Mol. Cell. Cardiol.* **67**, 1–11 (2014).
923 14. Tang, K.-J. *et al.* Focal Adhesion Kinase Regulates the DNA Damage Response and Its
924 Inhibition Radiosensitizes Mutant KRAS Lung Cancer. *Clin. Cancer Res. Off. J. Am.*
925 *Assoc. Cancer Res.* **22**, 5851–5863 (2016).
926 15. Tavora, B. *et al.* Endothelial-cell FAK targeting sensitizes tumours to DNA-damaging
927 therapy. *Nature* **514**, 112–116 (2014).
928 16. Ma, Z. *et al.* Role of BCLAF-1 in PD-L1 stabilization in response to ionizing irradiation.
929 *Cancer Sci.* **112**, 4064–4074 (2021).
930 17. Shao, A. *et al.* Bclaf1 is a direct target of HIF-1 and critically regulates the stability of HIF-
931 1α under hypoxia. *Oncogene* **39**, 2807–2818 (2020).
932 18. Ramanathan, A., Savol, A., Burger, V., Chennubhotla, C. S. & Agarwal, P. K. Protein
933 conformational populations and functionally relevant substates. *Acc. Chem. Res.* **47**, 149–
934 156 (2014).
935 19. Ha, J.-H. & Loh, S. N. Protein conformational switches: from nature to design. *Chem.*

Weinh. Bergstr. Ger. **18**, 7984–7999 (2012).
20. Forman-Kay, J. D., Ditlev, J. A., Nosella, M. L. & Lee, H. O. What are the distinguishing features and size requirements of biomolecular condensates and their implications for RNA-containing condensates? *RNA N. Y. N* **28**, 36–47 (2022).
21. Lietha, D. *et al.* Structural basis for the autoinhibition of focal adhesion kinase. *Cell* **129**, 1177–1187 (2007).
22. Sanders, D. W. *et al.* Competing Protein-RNA Interaction Networks Control Multiphase Intracellular Organization. *Cell* **181**, 306-324.e28 (2020).
23. Lin, Y., Protter, D. S. W., Rosen, M. K. & Parker, R. Formation and Maturation of Phase-Separated Liquid Droplets by RNA-Binding Proteins. *Mol. Cell* **60**, 208–219 (2015).
24. Jumper, J. *et al.* Highly accurate protein structure prediction with AlphaFold. *Nature* **596**, 583–589 (2021).
25. Abramson, J. *et al.* Accurate structure prediction of biomolecular interactions with AlphaFold 3. *Nature* **630**, 493–500 (2024).
26. Yu, Z. *et al.* BCLAF1 binds SPOP to stabilize PD-L1 and promotes the development and immune escape of hepatocellular carcinoma. *Cell. Mol. Life Sci. CMLS* **81**, 82 (2024).
27. Sarras, H., Alizadeh Azami, S. & McPherson, J. P. In search of a function for BCLAF1. *ScientificWorldJournal* **10**, 1450–1461 (2010).
28. Alberti, S. & Hyman, A. A. Biomolecular condensates at the nexus of cellular stress, protein aggregation disease and ageing. *Nat. Rev. Mol. Cell Biol.* **22**, 196–213 (2021).
29. Snead, W. T. & Gladfelter, A. S. The Control Centers of Biomolecular Phase Separation: How Membrane Surfaces, PTMs, and Active Processes Regulate Condensation. *Mol. Cell* **76**, 295–305 (2019).
30. Hatos, A., Tosatto, S. C. E., Vendruscolo, M. & Fuxreiter, M. FuzDrop on AlphaFold: visualizing the sequence-dependent propensity of liquid-liquid phase separation and aggregation of proteins. *Nucleic Acids Res.* **50**, W337–W344 (2022).
31. Liu, J. X. *et al.* Liquid-liquid phase separation within fibrillar networks. *Nat. Commun.* **14**, 6085 (2023).
32. Alshareedah, I., Kaur, T. & Banerjee, P. R. Methods for characterizing the material properties of biomolecular condensates. *Methods Enzymol.* **646**, 143–183 (2021).
33. Quan, M. D., Liao, S.-C. J., Ferreon, J. C. & Ferreon, A. C. M. Fluorescence Lifetime Imaging Microscopy of Biomolecular Condensates. *Methods Mol. Biol. Clifton NJ* **2563**, 135–148 (2023).
34. Filomeni, G., De Zio, D. & Cecconi, F. Oxidative stress and autophagy: the clash between damage and metabolic needs. *Cell Death Differ.* **22**, 377–388 (2015).
35. Scandalios, J. G. Oxidative stress: molecular perception and transduction of signals triggering antioxidant gene defenses. *Braz. J. Med. Biol. Res. Rev. Bras. Pesqui. Medicas E Biol.* **38**, 995–1014 (2005).
36. Hirose, T., Ninomiya, K., Nakagawa, S. & Yamazaki, T. A guide to membraneless organelles and their various roles in gene regulation. *Nat. Rev. Mol. Cell Biol.* **24**, 288–304 (2023).
37. Yoo, H., Bard, J. A. M., Pilipenko, E. V. & Drummond, D. A. Chaperones directly and efficiently disperse stress-triggered biomolecular condensates. *Mol. Cell* **82**, 741-755.e11 (2022).

38. Hornbeck, P. V. *et al.* PhosphoSitePlus, 2014: mutations, PTMs and recalibrations. *Nucleic Acids Res.* **43**, D512-520 (2015).
39. Sonoda, Y. *et al.* Anti-apoptotic role of focal adhesion kinase (FAK). Induction of inhibitor-of-apoptosis proteins and apoptosis suppression by the overexpression of FAK in a human leukemic cell line, HL-60. *J. Biol. Chem.* **275**, 16309–16315 (2000).
40. Clemente, C. F. M. Z. *et al.* Targeting focal adhesion kinase with small interfering RNA prevents and reverses load-induced cardiac hypertrophy in mice. *Circ. Res.* **101**, 1339–1348 (2007).
41. Focal adhesion kinase signaling in unexpected places - PubMed. https://pubmed.ncbi.nlm.nih.gov/28213315/.
42. Rodríguez-Fernández, J. L. Why do so many stimuli induce tyrosine phosphorylation of FAK? *BioEssays News Rev. Mol. Cell. Dev. Biol.* **21**, 1069–1075 (1999).
43. Autophosphorylation of the focal adhesion kinase, pp125FAK, directs SH2-dependent binding of pp60src - PubMed. https://pubmed.ncbi.nlm.nih.gov/7509446/.
44. Liu, Y., Yao, Z., Lian, G. & Yang, P. Biomolecular phase separation in stress granule assembly and virus infection. *Acta Biochim. Biophys. Sin.* **55**, 1099–1118 (2023).
45. Laflamme, G. & Mekhail, K. Biomolecular condensates as arbiters of biochemical reactions inside the nucleus. *Commun. Biol.* **3**, 773 (2020).
46. Ranganathan, S., Liu, J. & Shakhnovich, E. Different states and the associated fates of biomolecular condensates. *Essays Biochem.* **66**, 849–862 (2022).
47. Spegg, V. & Altmeyer, M. Biomolecular condensates at sites of DNA damage: More than just a phase. *DNA Repair* **106**, 103179 (2021).
48. Wen, Y. *et al.* Bclaf1 promotes angiogenesis by regulating HIF-1α transcription in hepatocellular carcinoma. *Oncogene* **38**, 1845–1859 (2019).
49. Shcherbakova, L., Pardo, M., Roumeliotis, T. & Choudhary, J. Identifying and characterising Thrap3, Bclaf1 and Erh interactions using cross-linking mass spectrometry. *Wellcome Open Res.* **6**, 260 (2021).
50. Pliss, A. *et al.* Cycles of protein condensation and discharge in nuclear organelles studied by fluorescence lifetime imaging. *Nat. Commun.* **10**, 455 (2019).
51. Case, L. B., De Pasquale, M., Henry, L. & Rosen, M. K. Synergistic phase separation of two pathways promotes integrin clustering and nascent adhesion formation. *eLife* **11**, e72588 (2022).
52. Akerfelt, M., Morimoto, R. I. & Sistonen, L. Heat shock factors: integrators of cell stress, development and lifespan. *Nat. Rev. Mol. Cell Biol.* **11**, 545–555 (2010).
53. Tyedmers, J., Mogk, A. & Bukau, B. Cellular strategies for controlling protein aggregation. *Nat. Rev. Mol. Cell Biol.* **11**, 777–788 (2010).
54. Mitrea, D. M., Mittasch, M., Gomes, B. F., Klein, I. A. & Murcko, M. A. Modulating biomolecular condensates: a novel approach to drug discovery. *Nat. Rev. Drug Discov.* **21**, 841–862 (2022).
55. Mateju, D. *et al.* An aberrant phase transition of stress granules triggered by misfolded protein and prevented by chaperone function. *EMBO J.* **36**, 1669–1687 (2017).
56. Kong, C.-Y. *et al.* Underlying the Mechanisms of Doxorubicin-Induced Acute Cardiotoxicity: Oxidative Stress and Cell Death. *Int. J. Biol. Sci.* **18**, 760–770 (2022).
57. Cappetta, D. *et al.* Oxidative Stress and Cellular Response to Doxorubicin: A Common

Factor in the Complex Milieu of Anthracycline Cardiotoxicity. *Oxid. Med. Cell. Longev.* **2017**, 1521020 (2017).

58. Zhang, X. *et al.* FNDC5 alleviates oxidative stress and cardiomyocyte apoptosis in doxorubicin-induced cardiotoxicity via activating AKT. *Cell Death Differ.* **27**, 540–555 (2020).
59. Song, I.-K. *et al.* Degradation of Redox-Sensitive Proteins including Peroxiredoxins and DJ-1 is Promoted by Oxidation-induced Conformational Changes and Ubiquitination. *Sci. Rep.* **6**, 34432 (2016).
60. Shang, F. & Taylor, A. Ubiquitin-proteasome pathway and cellular responses to oxidative stress. *Free Radic. Biol. Med.* **51**, 5–16 (2011).
61. Fan, Y., Qu, X., Ma, Y., Liu, Y. & Hu, X. Cbl-b promotes cell detachment via ubiquitination of focal adhesion kinase. *Oncol. Lett.* **12**, 1113–1118 (2016).
62. BommaReddy, R. R., Patel, R., Smalley, T. & Acevedo-Duncan, M. Effects of Atypical Protein Kinase C Inhibitor (DNDA) on Lung Cancer Proliferation and Migration by PKC-ι/FAK Ubiquitination Through the Cbl-b Pathway. *OncoTargets Ther.* **13**, 1661–1676 (2020).
63. Nandi, D., Tahiliani, P., Kumar, A. & Chandu, D. The ubiquitin-proteasome system. *J. Biosci.* **31**, 137–155 (2006).
64. Ranek, M. J. & Wang, X. Activation of the ubiquitin-proteasome system in doxorubicin cardiomyopathy. *Curr. Hypertens. Rep.* **11**, 389–395 (2009).
65. Lee, Y. Y., Yu, Y. B., Gunawardena, H. P., Xie, L. & Chen, X. BCLAF1 is a radiation-induced H2AX-interacting partner involved in γH2AX-mediated regulation of apoptosis and DNA repair. *Cell Death Dis.* **3**, e359 (2012).
66. Zhang, R. *et al.* Bclaf1 regulates c-FLIP expression and protects cells from TNF-induced apoptosis and tissue injury. *EMBO Rep.* **23**, e52702 (2022).
67. Frottin, F. *et al.* The nucleolus functions as a phase-separated protein quality control compartment. *Science* **365**, 342–347 (2019).
68. Galiani, S. *et al.* Super-resolution Microscopy Reveals Compartmentalization of Peroxisomal Membrane Proteins. *J. Biol. Chem.* **291**, 16948–16962 (2016).
69. Chomczynski, P. & Sacchi, N. Single-step method of RNA isolation by acid guanidinium thiocyanate-phenol-chloroform extraction. *Anal. Biochem.* **162**, 156–159 (1987).
70. Santos, M. D. M. *et al.* Simple, efficient and thorough shotgun proteomic analysis with PatternLab V. *Nat. Protoc.* **17**, 1553–1578 (2022).
71. Sun, J. *et al.* Precise prediction of phase-separation key residues by machine learning. *Nat. Commun.* **15**, 2662 (2024).